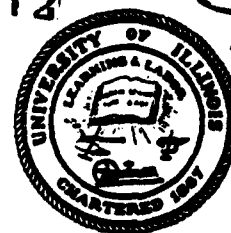
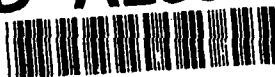


Department of Mechanical and  
Industrial Engineering  
University of Illinois at  
Urbana-Champaign  
Urbana, IL 61801

AEOSR-IR 94 0612



AD-A285 234



UILU-ENG 94-4011

## Annual Technical Report

### ARCJET PLASMA MODELING WITH EXPERIMENTAL VALIDATION

Herman Krier, Rodney L. Burton,  
T. W. Megli, S. A. Bufton, and N. T. Tillakos

Annual Contract Report Submitted to

Air Force Office of Scientific Research  
Dr. Mitat Birkan, Program Manager  
for research conducted during the period  
August 1, 1993 to July 31, 1994

under  
Contract F49620-92-J-0448 (Year 2)

September 1994

Approved for Public Release;  
Distribution Unlimited

DTIC QUALITY INSPECTED 2

94-31612



9410 04 01 6

UNCLASSIFIED

SECURITY CLASSIFICATION OF THIS PAGE

Dist: A

## REPORT DOCUMENTATION PAGE

Form Approved  
OMB No. 0704-0188

1a. REPORT SECURITY CLASSIFICATION Unclassified			1b. RESTRICTIVE MARKINGS None		
2a. SECURITY CLASSIFICATION AUTHORITY			3. DISTRIBUTION/AVAILABILITY OF REPORT Approved for public release; distribution is unlimited		
2b. DECLASSIFICATION/DOWNGRADING SCHEDULE			A		
4. PERFORMING ORGANIZATION REPORT NUMBER(S) UILU-ENG-94-4011					
5. MONITORING ORGANIZATION REPORT NUMBER(S) AFOSR-TR-			7a. NAME OF MONITORING ORGANIZATION AFOSR/NA		
6a. NAME OF PERFORMING ORGANIZATION University of Illinois at Urbana-Champaign		6b. OFFICE SYMBOL (If applicable) UIUC		7b. ADDRESS (City, State, and ZIP Code) 110 Duncan Ave; Suite B115 Bolling AFB, DC 20332-0001	
6c. ADDRESS (City, State, and ZIP Code) Department of Mechanical & Industrial Engr. 140 MEB; 1206 West Green Street; MC-244 Urbana, IL 61801		8a. NAME OF FUNDING/SPONSORING ORGANIZATION AFOSR/NA		9. PROCUREMENT INSTRUMENT IDENTIFICATION NUMBER F49620-92-J-0448 (Yr.2)	
8b. OFFICE SYMBOL (If applicable) AFOSR		10. SOURCE OF FUNDING NUMBERS		WORK UNIT ACCESSION NO.	
8c. ADDRESS (City, State, and ZIP Code) 110 Duncan Avenue; Suite B115 Bolling AFB, DC, 20332-0001		PROGRAM ELEMENT NO. U11007		PROJECT NO. 2308	
11. TITLE (Include Security Classification) Arcjet Plasma Modeling, with Experimental Verification		TASK NO. 178			
12. PERSONAL AUTHOR(S) H. Krier; R. L. Burton; T. W. Megli; S. A. Bufton; N. T. Tiliakos					
13a. TYPE OF REPORT Annual Report		13b. TIME COVERED FROM 7/30/93 TO 8/1/94		14. DATE OF REPORT (Year, Month, Day) 1994, Sept. 01	
15. PAGE COUNT 75					
16. SUPPLEMENTARY NOTATION					
17. COSATI CODES			18. SUBJECT TERMS (Continue on reverse if necessary and identify by block number)		
FIELD	GROUP	SUB-GROUP	Arcjet (Electric) Propulsion; Probe Diagnostics Non-Equilibrium Plasmas		
19. ABSTRACT (Continue on reverse if necessary and identify by block number)					
<p>We report for the first time thermal non-equilibrium (separate electron and gas temperatures) numerical results for a hydrazine arcjet. All viscous flow properties are considered, assuming laminar axisymmetric flow. The model includes anode temperature distribution, and the electrical conductivity is coupled to the flow properties, allowing for a self-consistent current distribution. The numerical solution algorithm employs the compressible form of the PISO algorithm to solve the continuity and momentum equations. Run time is a few hours on a Convex C240 Mainframe with a 44 x 24 grid. Numerical results are presented for low power hydrogen and hydrazine thrusters.</p> <p>[Continued, p.ii]</p>					
20. DISTRIBUTION/AVAILABILITY OF ABSTRACT <input checked="" type="checkbox"/> UNCLASSIFIED/UNLIMITED <input type="checkbox"/> SAME AS RPT. <input checked="" type="checkbox"/> DTIC USERS			21. ABSTRACT SECURITY CLASSIFICATION Unclassified		
22a. NAME OF RESPONSIBLE INDIVIDUAL Dr. Mitat Birkan			22b. TELEPHONE (Include Area Code) (202)767-4938		22c. OFFICE SYMBOL AFOSR/NA

Preliminary results of quadruple electrostatic probe measurements at the exit plane of a 1 kW hydrazine arcjet, including  $n_e$  and  $T_e$  profiles, are presented. The quadruple probe model includes the effects of  $T_e$  and  $n_e$  gradients across the probe volume to extract  $T_e$  and  $n_e$  radial profiles from the asymmetric raw probe data. A time-of-flight electrostatic probe technique for measuring heavy particle velocities is described which, when coupled with the quadruple probe data can yield radial profiles of  $n_e(r)$ ,  $T_e(r)$ ,  $T_i(r)$  and  $u_i(r)$

Experimental investigations of the energy deposition processes in the nozzle and constrictor regions of a 1-2 kW hydrazine arcjet are being performed. Electron number density and electron temperature measurements, using an array of flush-mounted Langmuir probes, will be made in the boundary layer, while emission spectroscopy will provide property measurements in the core flow. Current density measurements will also be made with the pin array, and will be compared with code results. Application of a steady-state magnetic field can be used to control arc attachment in a predictable manner.

**AFOSR**  
**ANNUAL TECHNICAL REPORT**  
**for the period 8/1/93 - 7/31/94**

**UILU-ENG-94-4011**

**Under Contract No.**  
**F49620-92-J-0448, Year 2**

**Arcjet Plasma Modeling with  
Experimental Validation**

Prepared by:

Herman Krier<sup>1</sup>  
Rodney L. Burton<sup>2</sup>  
Thomas W. Megli<sup>3</sup>  
Scott A. Bufton<sup>3</sup>  
Nicholas T. Tiliakos<sup>4</sup>

University of Illinois at Urbana-Champaign  
1206 West Green Street  
Urbana, IL 61801

Work supported by:

Air Force Office of Scientific Research  
Dr. Mitat Birkan is Program Manager  
AFOSR/NA, Building 410  
Bolling AFB, DC 20332-6448

Accession For	
NTIS	CRA&I <input checked="" type="checkbox"/>
DTIC	TAB <input type="checkbox"/>
Unannounced	<input type="checkbox"/>
Justification .....	
By .....	
Distribution /	
Availability Codes	
Dist	Avail and/or Special
A-1	

<sup>1</sup>Co-Principal Investigator; Faculty  
Department of Mechanical and  
Industrial Engineering

<sup>2</sup>Co-Principal Investigator; Faculty  
Department of Aeronautical and  
Astronautical Engineering

<sup>3</sup>Ph. D. Candidate  
Department of Mechanical and  
Industrial Engineering

<sup>4</sup>Ph. D. Candidate  
Department of Aeronautical  
and Astronautical Engineering

**APPROVED FOR PUBLIC RELEASE; DISTRIBUTION UNLIMITED**

September, 1994

## Table of Contents

	<b>Page</b>
Abstract	v
Overview/Introduction	vi
I. Two Temperature Modeling	1
II. Exit Plane Electrostatic Probe Studies	28
III. Arcjet Energy Deposition in the Constrictor and Nozzle	59
Appendix A Nitrogen Ion Density in Non-equilibrium Hydrazine Arcjets	73

## Abstract

We report for the first time thermal non-equilibrium (separate electron and gas temperatures) numerical results for a hydrazine arcjet. All viscous flow properties are considered, assuming laminar axisymmetric flow. The model includes anode temperature distribution, and the electrical conductivity is coupled to the flow properties, allowing for a self-consistent current distribution. The numerical solution algorithm employs the compressible form of the PISO algorithm to solve the continuity and momentum equations. Run time is a few hours on a Convex C240 Mainframe with a 44 x 24 grid. Numerical results are presented for low power hydrogen and hydrazine thrusters.

Preliminary results of quadruple electrostatic probe measurements at the exit plane of a 1 kW hydrazine arcjet, including  $n_e$  and  $T_e$  profiles, are presented. The quadruple probe model includes the effects of  $T_e$  and  $n_e$  gradients across the probe volume to extract  $T_e$  and  $n_e$  radial profiles from the asymmetric raw probe data. A time-of-flight electrostatic probe technique for measuring heavy particle velocities is described which, when coupled with the quadruple probe data can yield radial profiles of  $n_e(r)$ ,  $T_e(r)$ ,  $T_i(r)$  and  $u_i(r)$

Experimental investigations of the energy deposition processes in the nozzle and constrictor regions of a 1-2 kW hydrazine arcjet are being performed. Electron number density and electron temperature measurements, using an array of flush-mounted Langmuir probes, will be made in the boundary layer, while emission spectroscopy will provide property measurements in the core flow. Current density measurements will also be made with the pin array, and will be compared with code results. Application of a steady-state magnetic field can be used to control arc attachment in a predictable manner.

## Overview/Introduction -- Scientific Deficiencies and Barriers

The primary interest of the Air Force for arcjet propulsion is with storable propellants. The proposed research emphasizes gaseous mixtures of  $N_2$  and  $H_2$  for the simulation of  $N_2H_4$  and  $H_2$  arcjets. Because the arcjet is a low Reynolds number device ( $Re < 1000$ ), viscous behavior dominates energy transfer processes in the thermal and viscous nozzle boundary layers, which couples with multi-dimensional heat conduction in and from the massive conducting anode wall. Therefore, energy transfer must be described by coupled Navier-Stokes conservation relations which depend in a complex way on the fluid properties. To date, no single computational model can be said to describe accurately the entire physics of arcjet flows.

The energy transport from the plasma located in the equilibrium constrictor region of the arcjet is a strong function of the number density and distribution of electrons from ionized species. The degree of non-equilibrium can significantly alter the expected electron number density. The diffusion of species, particularly electrons, is likewise important. The electric current distribution, not known, is strongly coupled to the  $n_e$  and  $T_e$  distribution in the vicinity of the relatively cold constrictor and anode walls. Therefore non-equilibrium plays a dominant role, resulting in spatial variation in the current attachment and anode heating. The proper description of this aspect of arcjet nozzle flow has proven particularly difficult to achieve in numerical models of the arcjet.

An applied magnetic (B) field is known to alter electron drift and hence the current distribution and arcjet performance. Because of these interactions and because of the effect on swirl in the constrictor, a numerical model with applied B field can describe the complex physics of flow and energy transfer in this region of intense plasma heating. We expect to begin research in this area during the contract year.

All of the above factors vary significantly with power input (the scaling problem). Note that a given arcjet operates over a relatively narrow power range, and DC constricted arcjets as a class cannot be operated efficiently below 0.5 kW.

This technical report summarizes the research carried out by our group concerned with arcjet plasma propulsion. Section I describes the non-equilibrium plasma model and a detailed formulation for kinetic non-equilibrium. Section II describes the experimental research, where measurements of electron number density, electron temperature, Mach number and gas velocity are carried out by advanced Langmuir probes. Section III outlines our research with a modified 1-2 kW class arcjet, where surface Langmuir probes are used to investigate the constrictor and nozzle current attachment regions.

## Section 1: Two Temperature Modeling\*

### Nomenclature

$c_i$	mean thermal speed (m/s)
$C$	coulomb charge
$D$	effective diffusion coefficient ( $\text{m}^2/\text{s}$ )
$\text{elst}$	elastic energy transfer ( $\text{W}/\text{m}^3$ )
$h$	Planck's constant (J-s)
$h_i$	enthalpy of species $i$ (J/kg)
$I$	integrated total current (A)
$j$	current density ( $\text{A}/\text{m}^2$ )
$k_b$	Boltzmann's constant (J/K)
$k_c$	Coulomb constant ( $\text{Nm}^2/\text{C}^2$ )
$m_i$	mass of species $i$ (kg)
$M$	Mach number
$n_i$	number density of $i$ th species ( $\text{m}^{-3}$ )
$p$	pressure ( $\text{N}/\text{m}^2$ )
$P_\Omega$	ohmic power deposition (W)
$Q_{ij}$	collision cross section ( $\text{m}^2$ )
$T_a$	anode temperature (K)
$T_e$	electron temperature (K)
$T_g$	heavy species temperature (K)
$u$	axial velocity (m/s)
$U$	heavy species total particle energy (J)
$v$	radial velocity (m/s)
$\mathbf{v}$	velocity vector (m/s)
$V$	voltage (volts)
$w$	azimuthal swirl velocity (m/s)
$x, r, \theta$	cylindrical coordinates
$x_i$	mole fraction of species $i$
$x_{\text{mol}}$	mixture parameter in $x_{\text{mol}}\text{N}_2 + \text{H}_2$
$Z_i$	thermodynamic partition functions
$\epsilon_d$	dissociation energy (J)

---

\*Ph.D. Candidate, Thomas W. Megli, leads our group in developing a comprehensive model of the arcjet thermophysics.



$\lambda_h$	heavy species thermal conductivity (W/m-K)
$\Lambda_e$	Spitzer logarithm
$\mu$	gas viscosity (kg/ms)
$\epsilon_i$	ionization energy (J)
$\lambda_a$	anode thermal conductivity (W/m-K)
$\lambda_e$	electron thermal conductivity (W/m-K)
$\nu$	collision frequency (s <sup>-1</sup> )
$\rho$	mass density (kg/m <sup>3</sup> )
$\sigma$	electrical conductivity (mhos/m)
$\Phi_h$	viscous dissipation function (W/m <sup>3</sup> )
$\overline{\Omega}_{ij}$	collision integral (m <sup>2</sup> )

## 1.1 Introduction

Arcjet thrusters offer a significant advantage in specific impulse and therefore cost over conventional satellite propulsion systems. Low power 1-2 kW arcjets have been qualified for north-south station keeping, while higher power 20-30 kW designs are being considered for orbit transfer applications.<sup>1</sup>

Most arcjet design strategies to date have been empirical. The need for a more complete description of the complex physical processes in an arcjet has resulted in a variety of numerical models ranging from simplified one-dimensional design tools<sup>2</sup> to more complex two-dimensional descriptions of the gas dynamics and energy transfer processes.<sup>3-9</sup> Comprehensive arcjet models are required to (1) interpret experimental results, (2) understand the physical processes in regions of the thruster where diagnostic techniques are challenging, (3) improve arcjet performance and (4) ultimately scale the devices to higher power levels.

The fluid dynamics and energy transfer within the arcjet thruster are nonlinear and strongly coupled. The energy conversion mechanism for an arcjet is an electrical discharge, or arc, produced by a voltage difference between the thruster nozzle, which is the anode, and a conical electrode on the upstream side of the constrictor, which is the cathode. The arc current distribution depends on several factors in addition to the geometry. The distribution is coupled to the propellant mass flow rate, composition, thermal properties, electrical conductivity, and gas-dynamic properties.

Both chemical and thermal processes in the arcjet are described as non-equilibrium. Arc current is converted to electron thermal energy through ohmic dissipation. The electrons transfer thermal energy to heavy species in the arc plasma through collisions. This energy is then converted to

thrust as the fluid accelerates through the nozzle. In regions of low pressure and/or elevated ohmic heating, collisional coupling between electrons and heavy species may not establish equal gas and electron temperatures. Additionally, flow velocities are large so that fluid residence times in the nozzle are of the order of  $1\ \mu\text{s}$ ; much of the energy invested in dissociation and ionization is frozen. Pressures drop from roughly 1 atm at the constrictor to millitorr conditions at the exit; radial diffusion of electrons from the arc core is important in determining the arc structure.

The thrust and specific impulse produced by an arcjet are determined by several factors including the power transferred to the propellant, the extent of both kinetic and chemical non-equilibrium, the propellant gas mixture, and the arcjet nozzle geometry. Other factors which contribute to the overall performance include heat loss to the anode and the voltage sheaths at the electrodes. A comprehensive model of an arcjet thruster is therefore highly complex, including plasmadynamic, fluid dynamic, and surface and volumetric heat transfer phenomena.

This paper describes the formulation of a self-consistent arcjet model. In section 1.2 the kinetic non-equilibrium model is described, and in section 1.3 the numerical solution method is presented. Numerical results are presented in section 1.4. Non-LTE solutions are presented for both hydrogen and hydrazine cases.

The complete arcjet model will ultimately include detailed descriptions of kinetic non-equilibrium, finite rate chemistry, radiation transfer, and species diffusion. The model discussed here focuses on the kinetic non-equilibrium aspects of arcjet thrusters, and will provide a baseline comparison for future research including both kinetic and chemical non-equilibrium.

## 1.2 Model

An axisymmetric, steady state, laminar, two temperature kinetic non-equilibrium model is formulated for a direct current arcjet with flow swirl, a variable nozzle geometry, and a variable mixture of nitrogen and hydrogen. The model predicts thrust, specific impulse, and internal fields for pressure  $p$ , density  $\rho$ , and both electron  $T_e$  and heavy species  $T_g$  temperatures. Additionally, the model also predicts the current density distribution  $j$ , voltage potential  $V$ , and velocity components  $u$ ,  $v$ , and  $w$ .

The details of the model are presented in six sections below as: (1) the fluid dynamic equations, (2) the energy equations, (3) the electromagnetic equations, (4) the species number density computation, (5) transport coefficients, and (6) boundary conditions. Since an azimuthal velocity component  $w$ , or flow swirl, is included in the model, an azimuthal momentum equation must be included and a term containing  $w$  is included in the radial momentum equation. The arcjet geometry is described as  $(x,r,\theta)$  where  $x$  is the axial coordinate,  $r$  is the radial coordinate, and  $\theta$  is the azimuthal coordinate.

## 1. Fluid Dynamic Equations

The viscous fluid dynamic equations are summarized below:

Axial momentum:

$$\frac{\partial(\rho u)}{\partial x} + \frac{1}{r} \frac{\partial(r \rho u v)}{\partial r} = \frac{4}{3} \frac{\partial}{\partial x} \left( \mu \frac{\partial u}{\partial x} \right) + \frac{1}{r} \frac{\partial}{\partial r} \left( \mu r \frac{\partial u}{\partial r} \right) - \frac{2}{3} \frac{\partial}{\partial x} \left( \mu \frac{\partial v}{\partial r} \right) - \frac{2}{3r} \frac{\partial(\mu v)}{\partial x} + \frac{1}{r} \frac{\partial}{\partial r} \left( \mu r \frac{\partial v}{\partial x} \right) - \frac{\partial p}{\partial x} \quad (1)$$

Radial momentum:

$$\begin{aligned} \frac{\partial(\rho u v)}{\partial x} + \frac{1}{r} \frac{\partial(r \rho v v)}{\partial r} = & \frac{\partial}{\partial x} \left( \mu \frac{\partial v}{\partial x} \right) + \frac{4}{3r} \frac{\partial}{\partial r} \left( \mu r \frac{\partial v}{\partial r} \right) + \frac{\partial}{\partial x} \left( \mu \frac{\partial u}{\partial r} \right) + \frac{2\mu}{3r} \frac{\partial u}{\partial x} - \frac{2v}{3r} \frac{\partial \mu}{\partial r} \\ & - \frac{4}{3} \frac{\mu v}{r^2} - \frac{2}{3r} \frac{\partial}{\partial r} \left( \mu r \frac{\partial u}{\partial x} \right) - \frac{\partial p}{\partial r} + \frac{\rho w^2}{r} \end{aligned} \quad (2)$$

Azimuthal momentum ( $\partial p / \partial \theta = 0$ ):

$$\frac{\partial(\rho u (w r))}{\partial x} + \frac{1}{r} \frac{\partial}{\partial r} ((r \rho v + 2\mu)(w r)) = \frac{\partial}{\partial x} \left( \mu \frac{\partial (w r)}{\partial x} \right) + \frac{1}{r} \frac{\partial}{\partial r} \left( \mu r \frac{\partial (w r)}{\partial r} \right) \quad (3)$$

Axisymmetric continuity:

$$\frac{\partial}{\partial x}(\rho u) + \frac{1}{r} \frac{\partial}{\partial r}(r \rho v) = 0 \quad (4)$$

## 2. Energy Equations

The assumption of kinetic non-equilibrium gives separate energy equations for the electrons and heavy species. The electron energy equation is

$$\nabla \cdot \left( \frac{3}{2} k_B (n_e v - \frac{j}{e}) T_e \right) = \nabla \cdot (\lambda_e \nabla T_e) + m_e \nabla \cdot (h_e D_e \nabla n_e) - p_e \nabla \cdot v + \frac{j \cdot j}{\sigma} - \text{elst} - \text{radiation} \quad (5)$$

where 'elst' represents energy lost through elastic collisions with the heavy species,<sup>10</sup> and 'radiation' denotes optically thin radiation loss due to continuum bremsstrahlung radiation.<sup>11</sup> The elastic energy transfer source term is calculated as the sum of electron-atom and electron ion contributions as

$$\text{elst} = 3k_B(T_e - T_g)n_e m_e \sum_{\text{heavies}} \frac{\bar{v}_{es}}{m_s} \quad (6)$$

where the average collision frequencies between electrons and heavy species are calculated using the mean electron thermal speed and collision cross sections  $Q_{es}$  as<sup>11</sup>

$$\bar{v}_{es} = \sqrt{\frac{8k_b T_e}{\pi m_e}} n_s Q_{es} \quad (7)$$

where the electron ion cross sections are

$$Q_{ei} = \frac{\pi e^4 k_e^2 \ln \Lambda_e}{2(k_b T_e)^2} \quad (8)$$

Electron-H<sub>2</sub> and electron-N<sub>2</sub> collision frequencies are multiplied by energy loss factors to account for inelastic rotational and vibrational losses.<sup>12</sup>

The heavy species energy equation is

$$\nabla \cdot (n_h \mathbf{v} U) = \nabla \cdot (\lambda_h \nabla T_g) + \sum_{i \neq e} m_i \nabla \cdot (h_i D_i \nabla n_i) - p_h \nabla \cdot \mathbf{v} + \text{elst} + \Phi_h \quad (9)$$

where the particle energy  $U$  includes translational, rotational, vibrational, and bulk kinetic energy contributions as well as ground state ionization and dissociation potentials.

The anode temperature distribution is determined from the energy equation for heat conduction in a solid. Neglecting ohmic dissipation in the anode gives

$$\nabla \cdot (\lambda_a \nabla T_a) = 0 \quad (10)$$

where  $\lambda_a = \lambda_a(T_a)$ <sup>13</sup>.

### 3. Species Equations

The species number densities are computed assuming a two-temperature chemical equilibrium. With this formulation the species number densities are given as a function of the pressure  $p$ , the heavy species temperature  $T_g$ , and the electron temperature  $T_e$ . A plasma composition of N<sub>2</sub>, H<sub>2</sub>, N, H, N<sup>+</sup>, H<sup>+</sup>, and electrons is assumed. Dissociation and ionization equations are constructed from a generalized law of mass action as given by entropy maximization.<sup>14</sup> This yields the following equations for the nitrogen and hydrogen species:

$$\frac{n_H^2}{n_{H_2}} = \exp\left(-\frac{\epsilon_{d,H_2}}{k_b T_g}\right) \left(\frac{\pi m_H k_b T_g}{h^2}\right)^{3/2} \left(\frac{Z_{H,ex}^2}{Z_{H_2,ex} Z_{H_2,rot} Z_{H_2,vib}}\right) \quad (11a)$$

$$\frac{n_N^2}{n_{N_2}} = \exp\left(\frac{-\epsilon_{d,N_2}}{k_b T_g}\right) \left(\frac{\pi m_N k_b T_g}{h^2}\right)^{3/2} \left(\frac{Z_{N,ex}^2}{Z_{N_2,ex} Z_{N_2,rot} Z_{N_2,vib}}\right) \quad (11b)$$

$$\frac{n_e n_{H+}}{n_H} = 2 \exp\left(\frac{-\epsilon_{i,H}}{k_b T_e}\right) \left(\frac{\pi m_e k_b T_e}{h^2}\right)^{3/2} \left(\frac{Z_{H+,ex}}{Z_{H,ex}}\right) \quad (11c)$$

$$\frac{n_e n_{N+}}{n_N} = 2 \exp\left(\frac{-\epsilon_{i,N}}{k_b T_e}\right) \left(\frac{\pi m_e k_b T_e}{h^2}\right)^{3/2} \left(\frac{Z_{N+,ex}}{Z_{N,ex}}\right) \quad (11d)$$

In the above expressions, the excitation partition functions  $Z_{ex}$  are functions of  $T_e$ , while  $Z_{rot}$  and  $Z_{vib}$  are functions of  $T_g$ . Details for the calculation of the various partition functions can be found in References 11 and 15-17.

The plasma equation of state, quasi-neutrality, and the definition of the mixture parameter  $x_{mol}$  provide the additional relations required to solve for the seven unknown species. Note that the initial mixture composition is written as  $x_{mol}N_2 + H_2$  so that pure hydrogen ( $x_{mol}=0$ ), simulated hydrazine ( $x_{mol} = 1/2$ ) and simulated ammonia ( $x_{mol} = 1/3$ ) can be easily investigated:

$$x_{mol} = \frac{2n_{N_2} + n_N + n_{N+}}{2n_{H_2} + n_H + n_{H+}} \quad (12)$$

$$n_e = n_{H+} + n_{N+} \quad (13)$$

$$p = n_e k_b T_e + (n_{N_2} + n_{H_2} + n_N + n_H + n_e) k_b T_g \quad (14)$$

Equations (11) - (14) are iteratively solved using the Newton-Raphson method.<sup>18</sup> Results are indicated in Figures 1-1a through 1-1c, where the thermal equilibrium mole fractions for hydrogen ( $x_{mol} = 0$ ), hydrazine ( $x_{mol} = 0.5$ ), and nitrogen ( $x_{mol} \rightarrow \infty$ ) plasmas are shown. Hydrazine results at  $p = 1$  atm indicate nearly complete dissociation of  $H_2$  at gas temperatures above  $T_g = 5000$  K, followed by complete  $N_2$  dissociation above  $T_g = 8000$  K. The onset of ionization begins at approximately  $T_g = 10000$  K. Complete ionization is noted for temperatures in excess of  $T_g = 20000$  K. These calculations agree well with those of Capecchi and d'Agostino.<sup>19</sup>

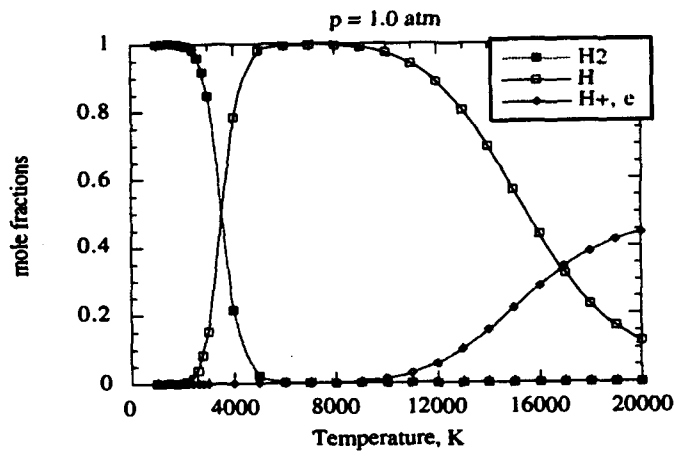


Figure 1-1a: Hydrogen mole fractions at  $p = 1$  atm.

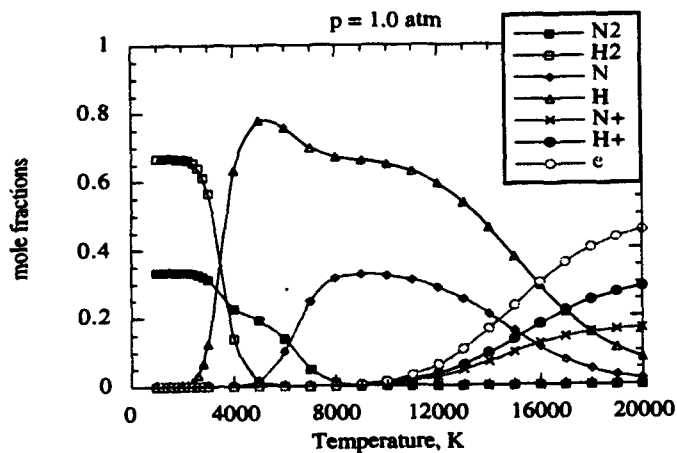


Figure 1-1b: Hydrazine mole fractions at  $p = 1$  atm.

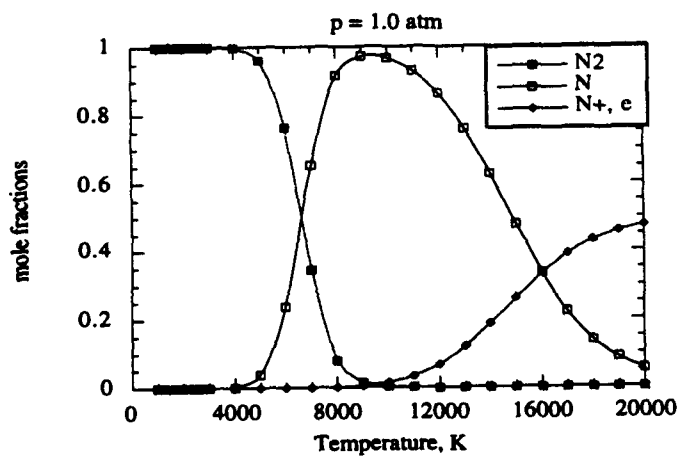


Figure 1-1c: Nitrogen mole fractions at  $p = 1$  atm

#### 4. Electromagnetic Equations

The calculation of the electrical current distribution is critical to understanding arc physics and poses a challenging problem in arcjet analysis. The current distribution is largely determined by the flow-field electrical conductivity, which is a strong function of the electron number density and temperature distribution. Local thermodynamic equilibrium (LTE) models must incorporate minimum electrical conductivity "floors" in the cool boundary layer region to avoid excessive voltage drops near the anode.<sup>3,6</sup> The artificial restriction that  $T_e = T_g$  results in an underprediction in the ionization (and therefore electron number density and  $\sigma$ ) in the boundary layer regions and a subsequent overprediction in power deposition. Hence, the conductivity floor is employed to provide agreement between the experimentally-observed and predicted power deposition.

Diffusion of electrons from the arc core towards the anode wall also elevates the electron number density and plays an important role in determining the boundary layer electrical conductivity. This has been demonstrated by Butler, Kull, and King, who show that the incorporation of diffusion provides a reasonable current distribution without imposing artificial restrictions on  $\sigma$  or the current attachment region.<sup>6</sup> However, the two-temperature solutions of Miller and Martinez-Sanchez<sup>4</sup> demonstrate that significant kinetic non-equilibrium, with elevated  $T_e$ , exists outside of the arc core in the constrictor region. These results indicate that both diffusion and increased ionization due to elevated  $T_e$  are important factors which determine the boundary layer electrical conductivity.

The correct approach to the arc attachment problem is to model the anode as an equipotential surface and allow the current distribution to be a model output which is independent of artificial restrictions. We are adopting a self-consistent approach for solving the current distribution and electric field simultaneously, for which the current distribution is properly coupled to the flow-field.

Assuming induced magnetic fields are negligible, and neglecting electron pressure gradient driving terms,<sup>12</sup> Ohm's law and current conservation are used to solve for the current density  $\mathbf{j}$  and voltage  $V$ :

$$-\nabla V = \mathbf{j}/\sigma \quad (15)$$

$$\nabla \cdot \mathbf{j} = 0 \quad (16)$$

## 5. Transport Coefficients

Transport coefficients for the present research are approximated using mean free path mixture rules taken from Mitchner and Kruger.<sup>20</sup> The viscosity is computed as

$$\mu = \frac{\sum_{i=1}^N \frac{n_i}{\sum_{j=1}^N n_j M_{ij}} \mu_i}{\sum_{j=1}^N n_j M_{ij}} \quad (17)$$

where  $M_{ij}$  is defined as

$$M_{ij} = \sqrt{\frac{2m_{ij}}{m_i} \frac{\overline{\Omega_{ij}^{(2,2)}}}{\overline{\Omega_{ii}^{(2,2)}}}} \quad (18)$$

and the pure species viscosity is

$$\mu_i = 1/2 m_i n_i c_i l_i \quad (19)$$

where  $c_i$  is the mean thermal speed,  $l_i$  is the mean free path, and  $\overline{\Omega_{ij}}$  is the collision integral for interaction between species  $i$  and  $j$ .

The translational contribution to the heavy species thermal conductivity is calculated using an equation similar to (17) with the pure species conductivity given as:

$$\lambda_i = \frac{15}{8} k_b n_i c_i l_i \left( \frac{9\gamma_i - 5}{15\gamma_i - 15} \right) \quad (20)$$

The electron thermal conductivity is

$$\lambda_e = \frac{2.4}{\left( 1 + \frac{\overline{\nu_{e-i}}}{\overline{\nu_{e-h}}} \right)} \frac{k_b^2 n_e T_e}{m_e \overline{\nu_{e-h}}} \quad (21)$$

where the electron-ion (e-i) and electron-heavy (e-h) effective collision frequencies are summed over the ionic and heavy species.

The electrical conductivity is calculated from



$$\sigma = \frac{n_e e^2}{m_e \sum_{i \neq e} n_i c_e \Omega_{e-i}^{-(1,1)}} \quad (22)$$

The effective diffusion coefficients  $D_i$  are calculated from

$$D_i = \frac{1 - x_i}{\sum_{j \neq i} x_j / D_{ij}} \quad (23)$$

where the  $D_{ij}$  are the binary mixture diffusion coefficients given as<sup>21</sup>

$$D_{ij} = \frac{3}{16 n \Omega_{ij}^{-(1,1)}} \left( \frac{2 k_b T (m_i + m_j)}{\pi m_i m_j} \right)^{1/2} \quad (24)$$

The electron and ion diffusion coefficients are modified to account for the ambipolar electric field.

Assuming  $\frac{\nabla n_e}{n_e} \approx \frac{\nabla n_{H^+}}{n_{H^+}} \approx \frac{\nabla n_{N^+}}{n_{N^+}}$ , the ambipolar diffusion coefficients for electrons,  $H^+$ , and  $N^+$  are:

$$D_{a,e} = \frac{D_e(\mu_{H^+} n_{H^+} + \mu_{N^+} n_{N^+}) + \mu_e(D_{H^+} n_{H^+} + D_{N^+} n_{N^+})}{\mu_e n_e + \mu_{H^+} n_{H^+} + \mu_{N^+} n_{N^+}} \quad (25)$$

$$D_{a,H^+} = \frac{D_{H^+}(\mu_e n_e + \mu_{N^+} n_{N^+}) + \mu_{H^+}(D_e n_e - D_{N^+} n_{N^+})}{\mu_e n_e + \mu_{H^+} n_{H^+} + \mu_{N^+} n_{N^+}} \quad (26)$$

$$D_{a,N^+} = \frac{D_{N^+}(\mu_e n_e + \mu_{H^+} n_{H^+}) + \mu_{N^+}(D_e n_e - D_{H^+} n_{H^+})}{\mu_e n_e + \mu_{H^+} n_{H^+} + \mu_{N^+} n_{N^+}} \quad (27)$$

where the mobilities  $\mu$  are calculated from  $\mu_i = \frac{e D_i}{k_b T_i}$ .

The collision integrals and cross-sections required for the above relations are obtained from References 22-27.

Equilibrium transport coefficients for hydrazine are shown in Figures 1-2 through 1-5. The heavy species viscosity, indicated in Fig. 1-2, varies widely due to the changing gas composition, with maxima at  $T_g = 8000, 10000, \text{ and } 12000 \text{ K}$  for pressures of  $p = 0.01, 0.1, \text{ and } 1 \text{ atm}$ . The maxima increase with pressure, indicating peak values of roughly  $\mu = 1.7 \times 10^{-4}, 2.0 \times 10^{-4}, \text{ and}$

$2.4 \times 10^{-4} \text{ N-s/m}^2$  respectively. Qualitatively similar results for the translational thermal conductivity are shown in Fig. 1-3.

The electron thermal conductivity, shown in Fig. 1-4, essentially vanishes for temperatures below 6000 K. For  $T > 6000 \text{ K}$   $\lambda_e$  increases monotonically. Electrical conductivities are shown in Fig. 1-5. For  $5000 \text{ K} < T < 9000 \text{ K}$ ,  $\sigma$  varies inversely with pressure. Above 9000 K,  $\sigma$  increases with pressure and temperature, indicating values at  $T = 20000 \text{ K}$  of  $\sigma = 10000, 12500$ , and  $15500 \text{ mhos/m}$  for pressures of  $p = 0.01, 0.1$ , and  $1 \text{ atm}$ .

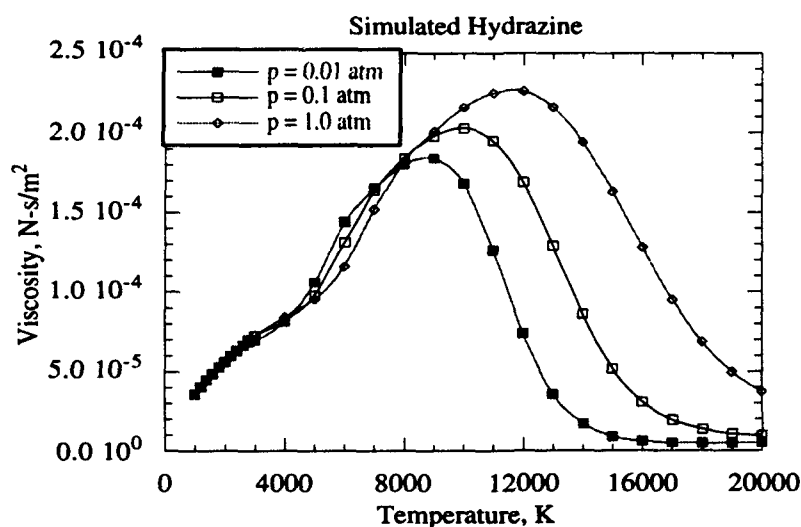


Figure 1-2: Viscosity versus temperature for hydrazine.

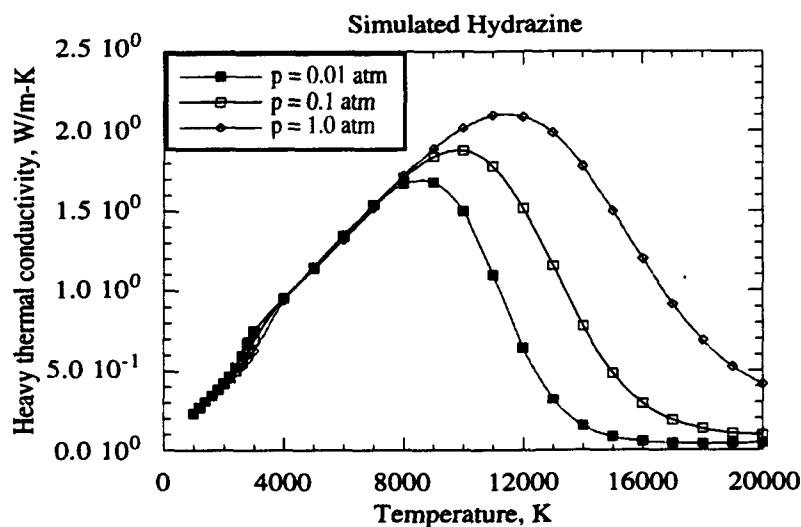


Figure 1-3: Translational thermal conductivity.

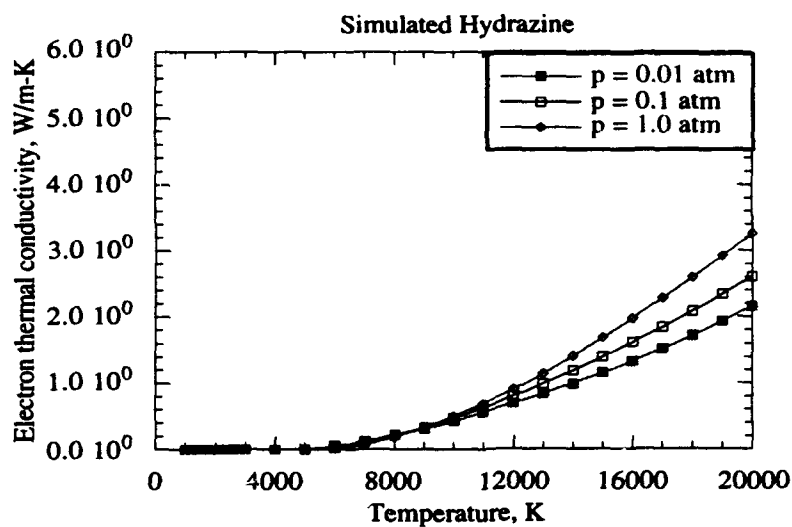


Figure 1-4: Electron thermal conductivity.

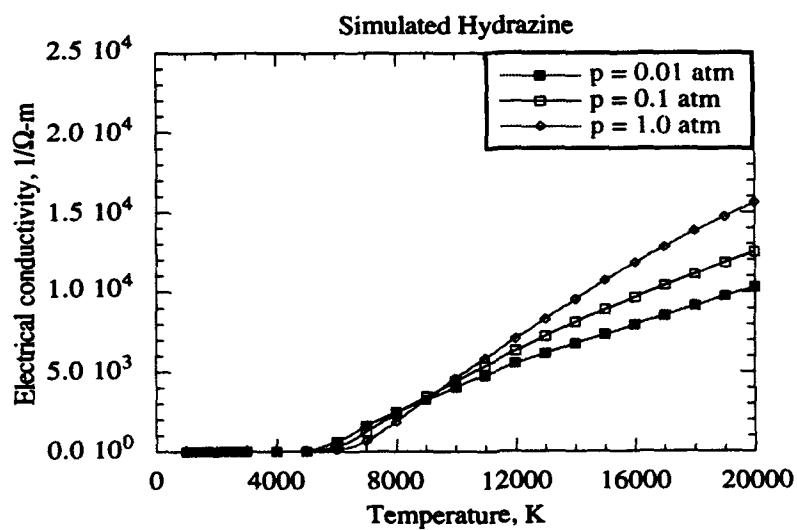


Figure 1-5: Electrical conductivity.

## 6. Boundary Conditions

The physical boundary conditions for the continuity, momentum, energy, and electromagnetic equations are summarized in Table I and Fig. 1-6. At the inflow boundary 1A, the flow is axial and the stagnation temperature  $T_t$  and stagnation pressure  $p_t$  are specified. The stagnation pressure is adjusted to obtain the desired mass flow rate. The static pressure  $p$  is extrapolated from the interior of the domain. The  $u$ -velocities and the inlet static temperatures are then computed from the isentropic stagnation property relations. The effects of flow swirl are incorporated by specifying the azimuthal inlet  $w$ -velocities as a fraction of the  $u$ -velocities. At the solid cathode 1C and anode 1D surfaces, no-slip conditions are employed. Zero radial gradients are specified on the center-line 1E.

At the outflow boundary 1B, since the boundary layer flow is subsonic, a low static pressure is specified. This is incorrect for supersonic flow. The effect of this condition on the solution will be systematically investigated; the correct exit pressure distribution would ultimately require the extension of the computational domain to include the plume. We are also considering a mixed boundary condition where the pressure is extrapolated for locally supersonic flow, and is fixed for locally subsonic flow.

The outflow  $u$ -velocities are updated to satisfy continuity using velocity corrections as given by discretized forms of the momentum and continuity equations for the exit plane. This is consistent with the numerical solution method discussed in section 1.3. Note that a zero electron temperature gradient is employed at the walls 1C and 1D. At low temperatures, the electron thermal conductivity approaches zero so that this boundary condition will have little effect on the results.<sup>28</sup>

The boundary conditions for the voltage are shown in Table I. The anode is modeled as an equipotential surface, while the cathode voltage is either equipotential or has a prescribed axial current distribution at the tip. Note that in this formulation the sheath voltage drops  $V_s$  have been uncoupled from the bulk plasma. The axial gradient of the voltage is set to zero at the inflow and outflow boundaries so that current is forced to attach within the arcjet nozzle. Recent radial electric field and  $\sigma$  measurements along the exit plane, showing the existence of roughly 1 A/cm<sup>2</sup> current density, suggest that this boundary condition may need refinement.<sup>29</sup>



Flow-Field Domain					
variable	1A	1B	1C	1D	1E
u	from stagnation properties	from momentum	= 0	= 0	$\frac{\partial u}{\partial r} = 0$
v	= 0	extrapolated	= 0	= 0	= 0
w	specified	extrapolated	= 0	= 0	= 0
T <sub>e</sub>	$\frac{\partial T_e}{\partial x} = 0$	extrapolated	$\frac{\partial T_e}{\partial \bar{n}} = 0$	$\frac{\partial T_e}{\partial \bar{n}} = 0$	$\frac{\partial T_e}{\partial r} = 0$
T <sub>g</sub>	from M and T <sub>t</sub>	extrapolated	specified	T <sub>g</sub> = T <sub>a</sub>	$\frac{\partial T_g}{\partial r} = 0$
P	extrapolated	specified	$\frac{\partial P}{\partial \bar{n}} = 0$	$\frac{\partial P}{\partial \bar{n}} = 0$	$\frac{\partial P}{\partial r} = 0$
V	$\frac{\partial V}{\partial x} = 0$	$\frac{\partial V}{\partial x} = 0$	V = V <sub>cat</sub> or j specified	V = V <sub>s</sub>	$\frac{\partial V}{\partial r} = 0$
Anode Domain					
variable	2A	2B	2C	2D	
T <sub>a</sub>	T <sub>a</sub> specified or $\frac{\partial T_a}{\partial x} = 0$	$\dot{q} = \epsilon \sigma (T_s^4 - T_{bg}^4)$	$\dot{q} = \lambda_h \frac{\partial T_g}{\partial \bar{n}} + j V_s$	$\dot{q} = \epsilon \sigma (T_s^4 - T_{bg}^4)$	

Table I: Boundary conditions.

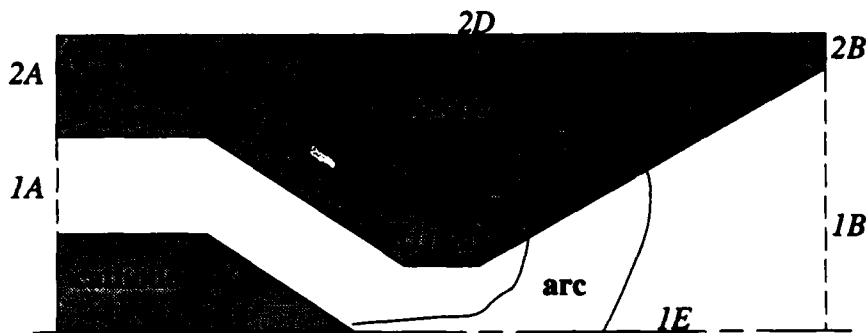


Figure 1-6: Schematic of fluid and anode domain boundaries.

The boundary conditions for the anode energy equation are also shown in Table I. On the outer surfaces 2B and 2D, the local heat flux is given by radiation to the surroundings at a specified background temperature  $T_{bg} \ll T_a$ . Along the anode surface 2C, the net heat flux is calculated as the sum of the heat flux due to conduction from the flow-field and the sheath losses given by the product of the local current density and the estimated sheath voltage drop  $V_s$ . Note that the radiation loss from the plasma to the anode is neglected in this formulation. Surface 2A is either a fixed temperature or zero heat flux boundary.

### 1.3 Numerical Solution Method

The solution method is structured around the global continuity and momentum equations. These are solved using a compressible form of the pressure-based PISO algorithm,<sup>30</sup> where the density variations are implicitly included in the pressure-correction procedure as described by Rhie.<sup>31</sup> Staggered velocity and scalar grids yield a well connected pressure field. Upstream weighted densities are employed to insure numerical stability.<sup>32</sup> The equations are discretized and power law differencing of convective and diffusive portions of the linearized coefficients preserves numerical stability in regions of the flow where convection dominates. The solution process is iterative and values for the field variables from the latest iteration are used to linearize the source terms. Under-relaxation is employed so that updated solutions are fractionally added to the solution from the previous iteration. The governing equations are transformed into natural coordinates and solved on a uniform computational mesh.

Fig. 1-7 illustrates the solution algorithm. The energy equations are solved to update gas, electron, and anode temperature fields. The species number densities, transport coefficients, and source terms are then updated using the latest available temperatures and pressures. The continuity and momentum equations are solved to update the pressure and velocity fields. Finally, the voltage and current density distributions are updated. Iterations are continued until the discretized equation residuals are converged.

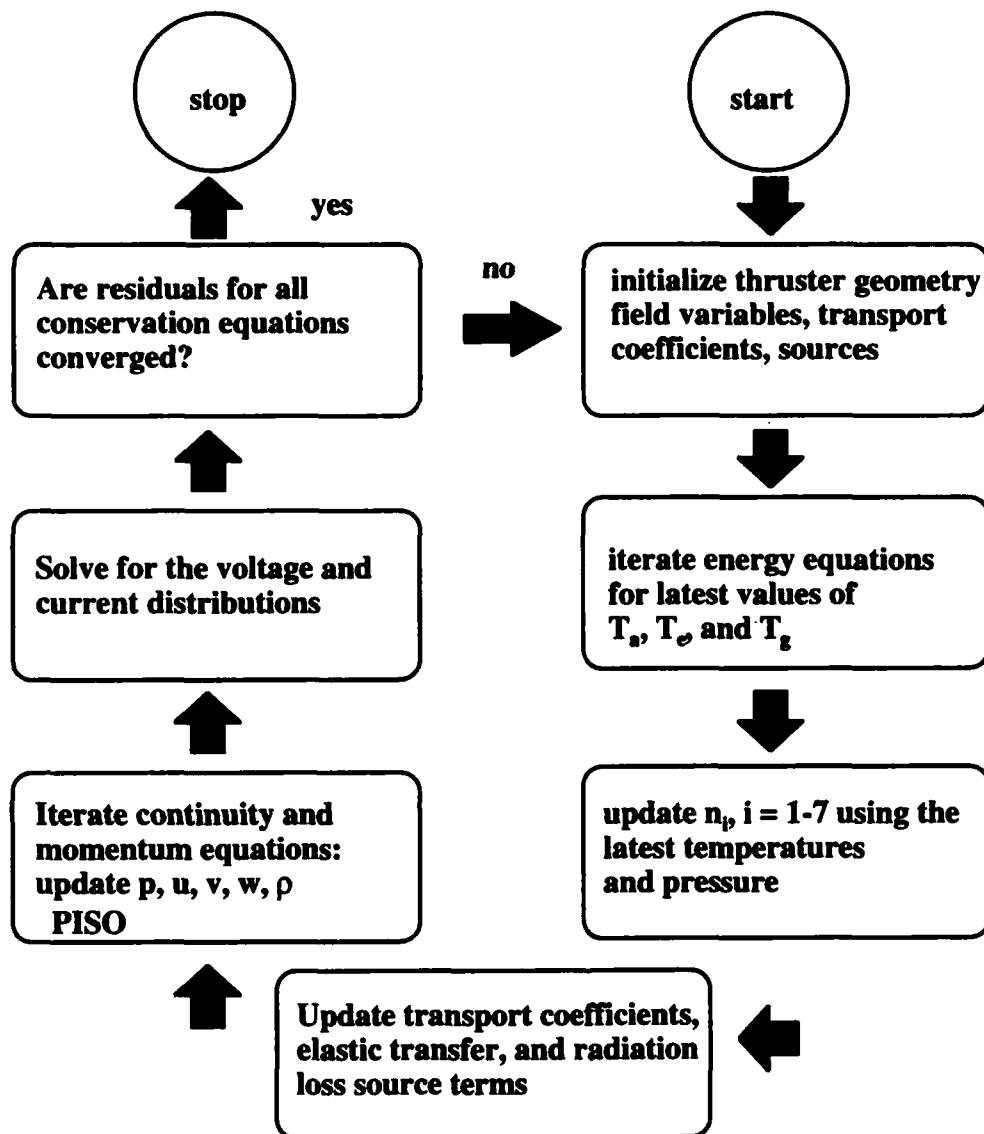


Figure 1-7: Numerical solution algorithm.

## 1.4 Model Results

Initial results for the arcjet model were summarized by Megli, et al.<sup>33</sup> An LTE solution was given for a low-power hydrogen arcjet flow. The vanishing near-anode electrical conductivity  $\sigma$  inherent in the assumption of thermal and chemical equilibrium required the use of an analytical electrical conductivity to avoid unreasonably high ohmic power depositions. Both the anode heat transfer and the current distribution were decoupled from the flow.

Recent modeling progress has yielded thermal non-equilibrium solutions including coupled electrical conductivity and anode heat transfer.  $T_e > T_g$  predicts a finite near-anode electrical conductivity. This is clearly illustrated in Fig. 1-8, where the electrical conductivity for a hydrogen plasma at  $p = 1$  atm is shown for various combinations of  $T_g$  and  $T_e$ . With  $T_e = T_g$ ,  $\sigma$  is essentially zero for  $T_g < 4000$  K. As the ratio of gas to electron temperature is increased, the increased ionization elevates  $\sigma$  from the value predicted assuming LTE ( $T_e/T_g = 1.0$ ). For example, for  $T_g = 6000$  K,  $\sigma$  increases from roughly  $\sigma = 50$  mhos/m to  $\sigma = 5000$  mhos/m as  $T_e$  is increased to 12000 K ( $T_e/T_g = 2.0$ ).

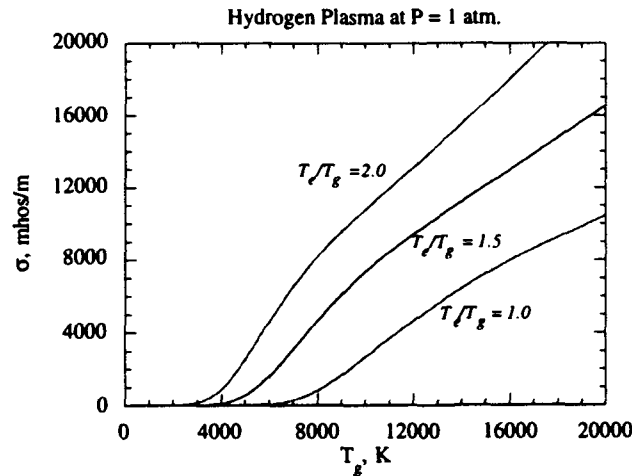


Figure 1-8: The effect of kinetic non-equilibrium on the electrical conductivity.

The numerical parameters and results for three non-LTE solutions are summarized in Table II. For these cases, flow swirl, species diffusion contributions to the heat flux vector, and viscous dissipation  $\Phi_h$  are neglected. The exit pressure is constant at  $p = 25$  Pa. The temperature of the upstream anode surface 2A is fixed at  $T = 1000$  K, and the cathode temperature increases linearly from  $T = 1000$  K at the inlet to  $T = 3000$  K at the tip. Also, a constant anode fall of  $V_s = 7.0$  volts is assumed, and a uniform axial current is specified on the cathode tip. The emissivity of the anode is  $\epsilon = 0.32$ , and the stagnation temperature of the inflow is  $T_t = 1000$  K.

case	propellant	$p_t$ at inlet (Pa)	I (amps)	$\dot{m}$ (mg/s)	$P_\Omega$ (W)	$I_{sp}$ (s)
1	H <sub>2</sub>	240000	15	17.1	771	912
2	H <sub>2</sub>	240000	20	12.6	1044	1011
3	N <sub>2</sub> H <sub>4</sub>	475000	15	48.5	949	613

Table II: Parameters for non-LTE simulations.



For each case, a grid with 44 uniformly spaced axial nodes is used. The fluid and anode domains contain 11 and 12 radial nodes as indicated in Fig. 1-9. These grids clearly warrant refinement in the constrictor region; however, the coarser grids minimize the computational effort required, and the solutions reveal interesting non-equilibrium physics present in arcjet flows. Additional cases on refined grids are in progress. Computations are performed on the UIUC Convex C-240 mainframe computer.

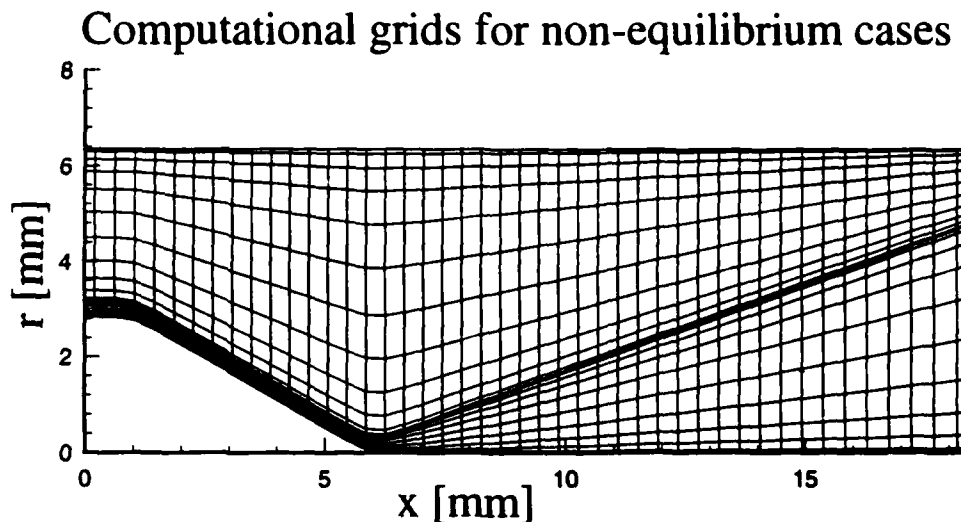


Figure 1-9: Computational grids used for the non-LTE solution.

Gas temperature contours are shown in Figures 1-10a through 1-10c. For the low power hydrogen case 1 ( $\frac{P_{\Omega}}{\dot{m}} = 45 \text{ MJ/kg}$ ), a peak temperature of roughly  $T_g = 7500 \text{ K}$  is noted near the cathode tip. The gas temperature then decreases to  $T_g = 1500 \text{ K}$  as the flow accelerates along the centerline to the nozzle exit. The higher  $\frac{P_{\Omega}}{\dot{m}} = 83 \text{ MJ/kg}$  indicated for case 2 gives a higher temperature of  $T_g = 9000 \text{ K}$  in the constrictor and a higher centerline exit temperature of  $T_g = 2800 \text{ K}$ . For the hydrazine case 3 ( $\frac{P_{\Omega}}{\dot{m}} = 20 \text{ MJ/kg}$ ), the gas temperature in the constrictor is roughly  $T_g = 12000 \text{ K}$  and decreases to roughly  $2900 \text{ K}$  at the exit.

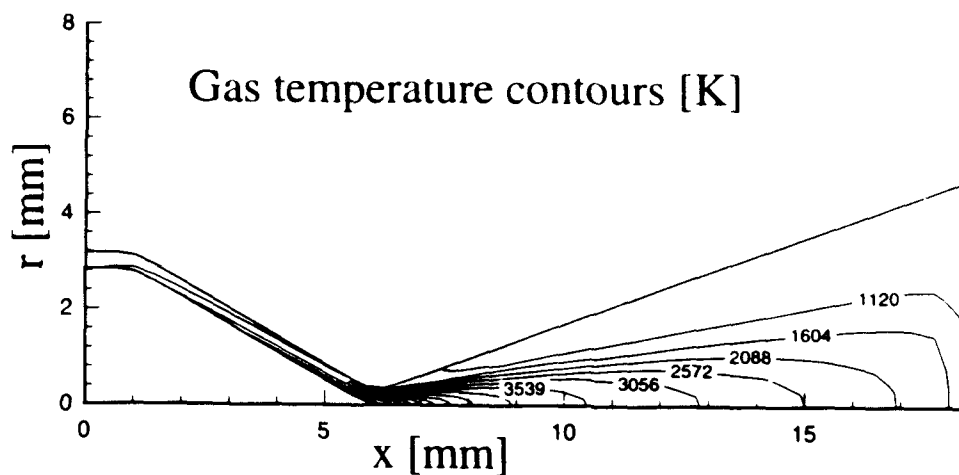


Figure 1-10a: Gas temperature contours for case 1 ( $\text{H}_2$  at  $\frac{P_{\Omega}}{\dot{m}} = 45 \text{ MJ/kg}$ ).

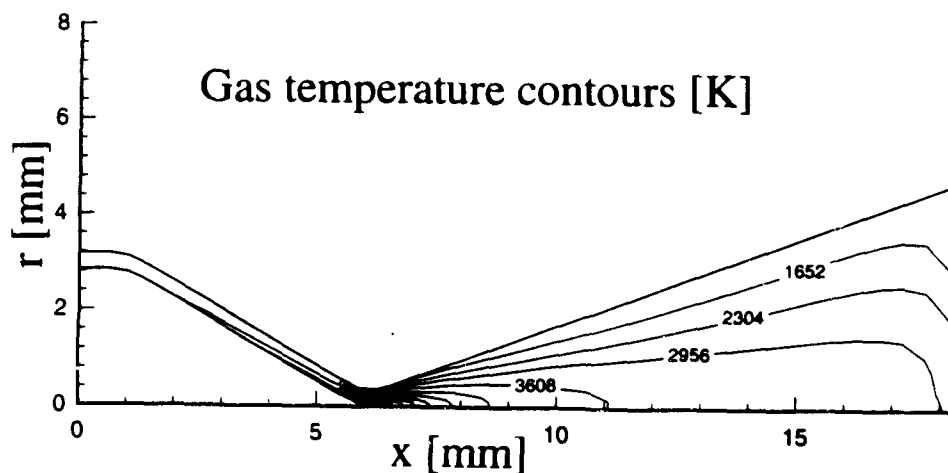


Figure 1-10b: Gas temperature contours for case 2 ( $\text{H}_2$  at  $\frac{P_{\Omega}}{\dot{m}} = 83 \text{ MJ/kg}$ ).

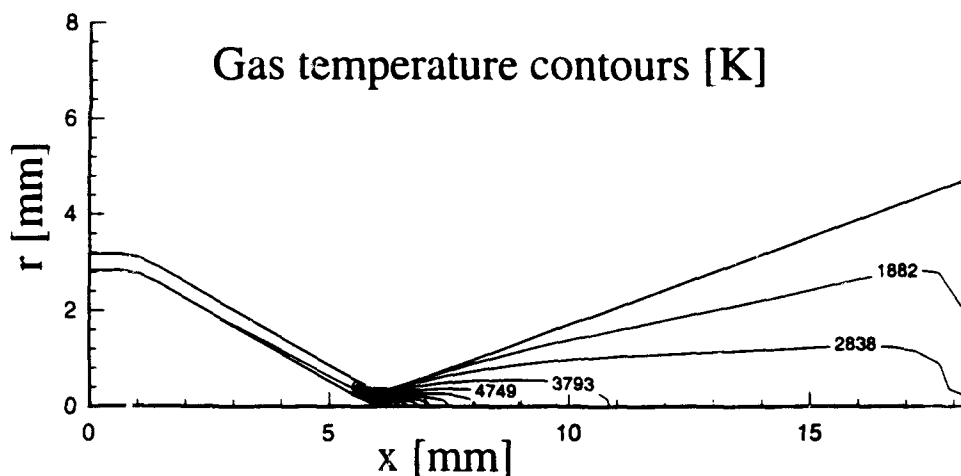


Figure 1-10c: Gas temperature contours for case 3 ( $\text{N}_2\text{H}_4$  at  $\frac{P_{\Omega}}{\dot{m}} = 20 \text{ MJ/kg}$ ).

Thermal non-equilibrium is indicated in Figures 1-11a through 1-11c, where contours of  $T_e/T_g$  are shown. A comparison of Figures 1-11a and 1-11b indicates that increasing the power deposition from  $\frac{P\Omega}{\dot{m}} = 45 \text{ MJ/kg}$  to  $\frac{P\Omega}{\dot{m}} = 83 \text{ MJ/kg}$  drives the flow towards thermal equilibrium. Increased ionization improves the collisional coupling between the electrons and the gas. The flow near the anode is highly non-equilibrium with maxima just downstream of the constrictor of roughly  $T_e/T_g = 18, 9, \text{ and } 8$  indicated for cases 1-3 respectively. The elevated  $T_e$  in this region produces the ionization necessary for a reasonable near-anode  $\sigma$  prediction.

Axial velocity contours are shown in Figures 1-12a through 1-12c. For the hydrogen flows, peak centerline velocities of roughly  $u = 16000 \text{ m/s}$  and  $u = 18000 \text{ m/s}$  are indicated at an axial location of  $x = 3 - 4 \text{ mm}$  downstream of the cathode tip. Interestingly, the centerline velocity increases monotonically toward the nozzle exit for the hydrazine case.

#### Anode Temperature Distributions

Figures 1-13a through 1-13c illustrate the anode temperature distributions. Increasing the power deposition and current increases the thermal loading, as peak temperatures near the constrictor of roughly  $T_a = 1190$  and  $T_a = 1460 \text{ K}$  are noted for cases 1 and 2. This is clearly illustrated in Fig 1-14, where the conductive and sheath loss contributions to the anode heat flux are shown. Maxima in conduction losses of  $q = 2500$  and  $q = 8500 \text{ W/cm}^2$  occur at the constrictor entrance for  $\frac{P\Omega}{\dot{m}} = 45 \text{ MJ/kg}$  and  $\frac{P\Omega}{\dot{m}} = 83 \text{ MJ/kg}$  respectively. Peak sheath losses of  $q = 3000$  and  $q = 6400 \text{ W/cm}^2$  are noted. Since a constant anode fall of  $V_s = 7.0 \text{ Volts}$  is assumed, the sheath losses are simply proportional to the local current density, and the maxima occur just downstream of the constrictor where the majority of the current attaches.

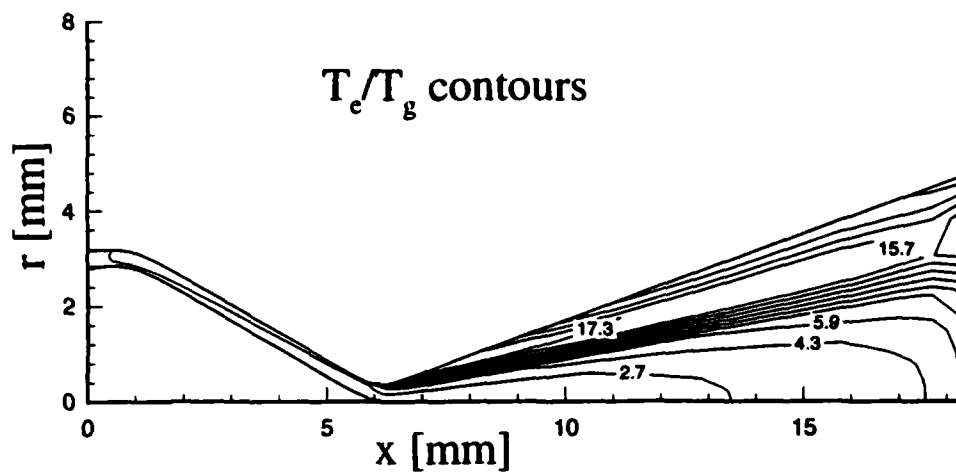


Figure 1-11a:  $T_e/T_g$  contours for case 1 ( $H_2$  at  $\frac{P_{\Omega}}{\dot{m}} = 45$  MJ/kg).

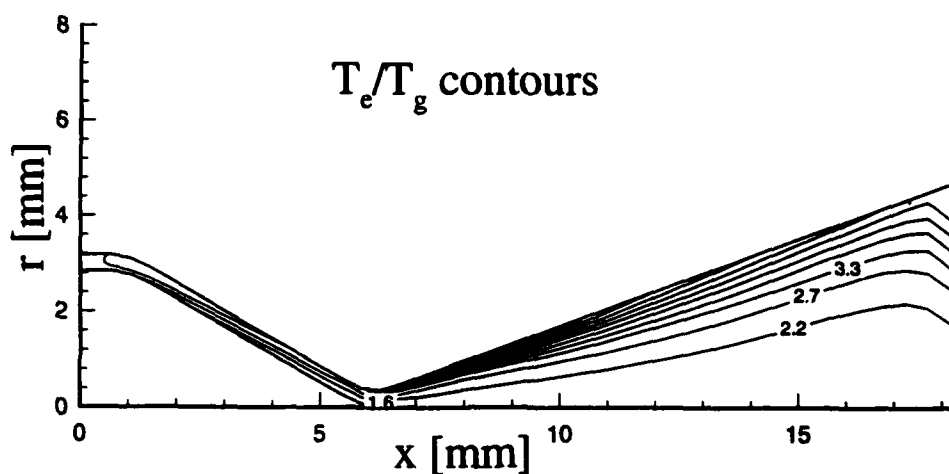


Figure 1-11b:  $T_e/T_g$  contours for case 2 ( $H_2$  at  $\frac{P_{\Omega}}{\dot{m}} = 83$  MJ/kg).

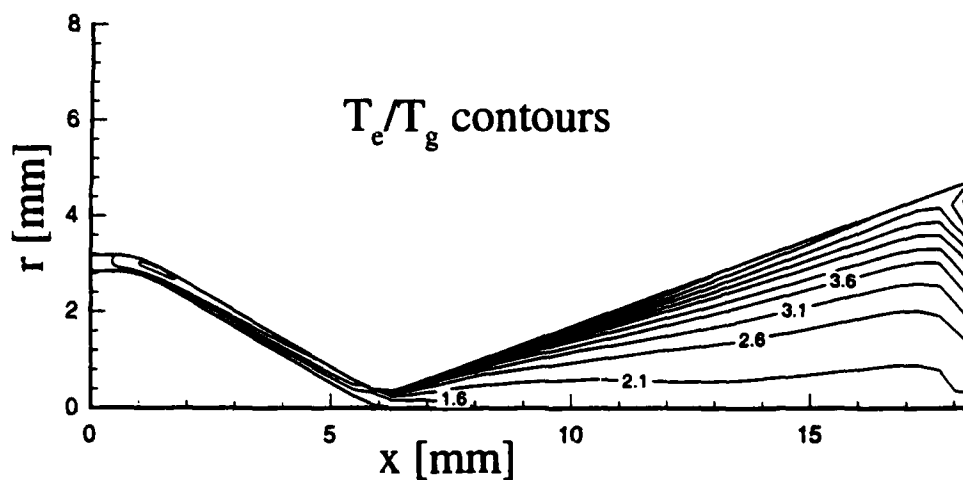


Figure 1-11c:  $T_e/T_g$  contours for case 3 ( $N_2H_4$  at  $\frac{P_{\Omega}}{\dot{m}} = 20$  MJ/kg).

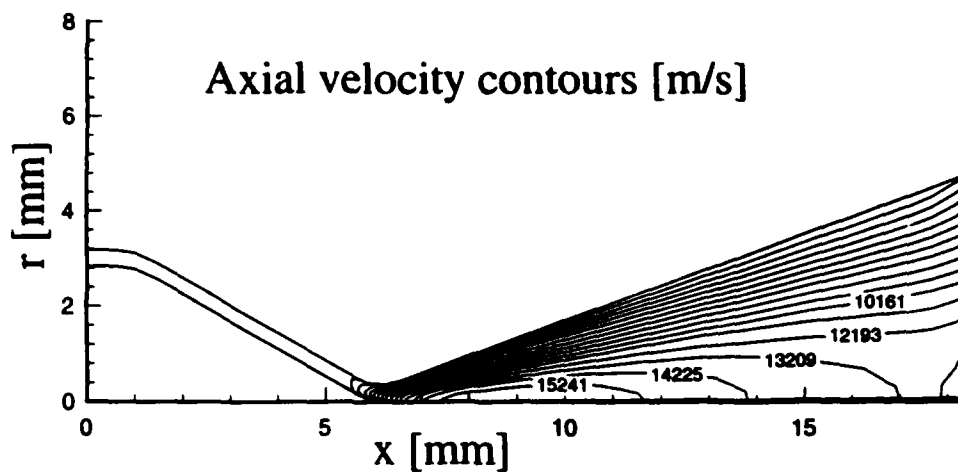


Figure 1-12a: Axial velocity  $u$  contours for case 1 ( $\text{H}_2$  at  $\frac{P_\Omega}{\dot{m}} = 45 \text{ MJ/kg}$ ).

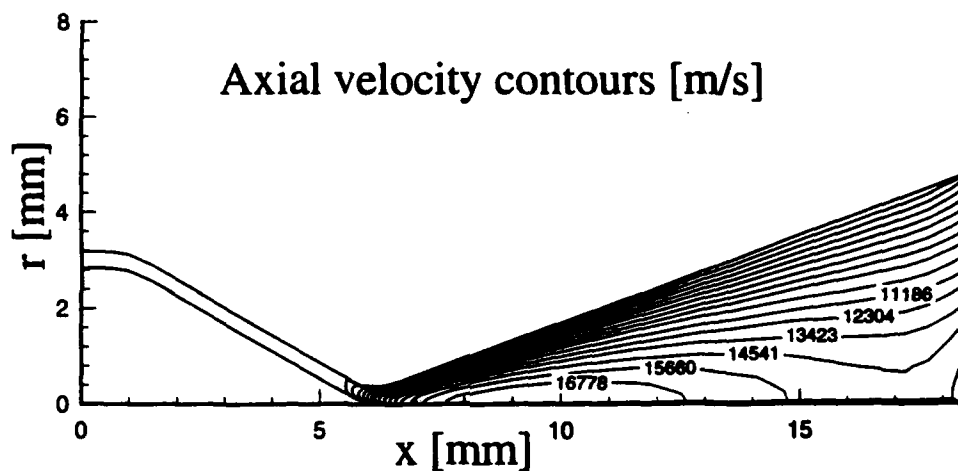


Figure 1-12b: Axial velocity  $u$  contours for case 2 ( $\text{H}_2$  at  $\frac{P_\Omega}{\dot{m}} = 83 \text{ MJ/kg}$ ).

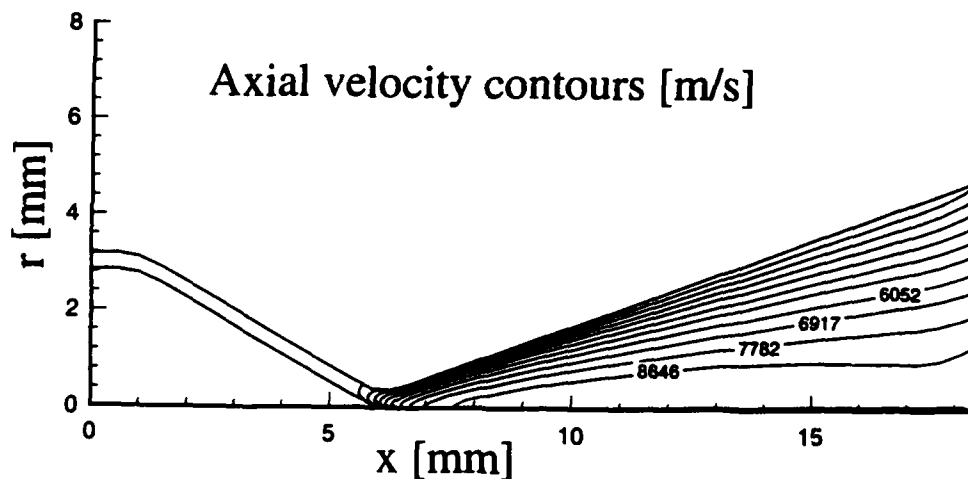


Figure 1-12c: Axial velocity  $u$  contours for case 3 ( $\text{N}_2\text{H}_4$  at  $\frac{P_\Omega}{\dot{m}} = 20 \text{ MJ/kg}$ ).

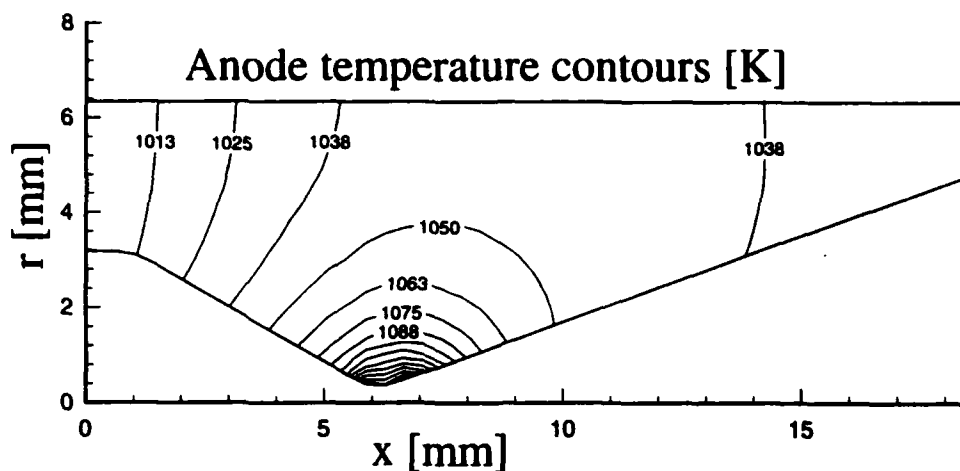


Figure 1-13a: Anode temperature distribution for case 1 ( $H_2$  at  $\frac{P_{\Omega}}{m} = 45$  MJ/kg).

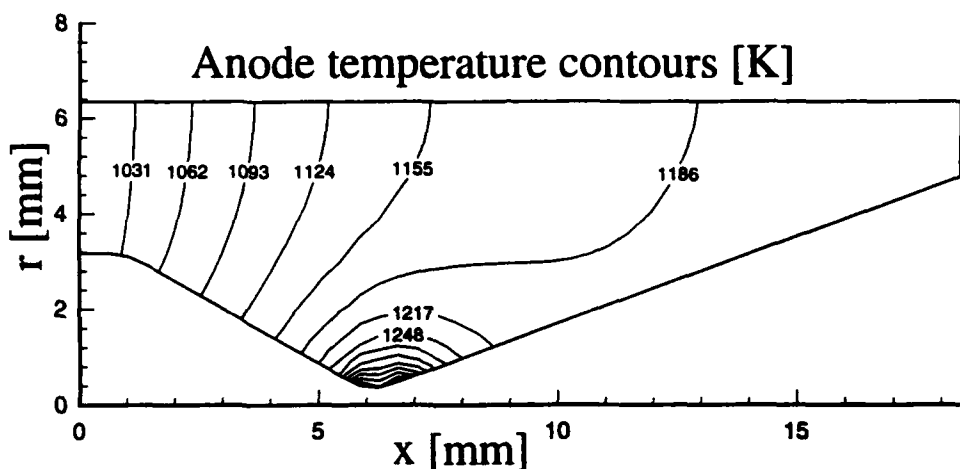


Figure 1-13b: Anode temperature distribution for case 2 ( $H_2$  at  $\frac{P_{\Omega}}{m} = 83$  MJ/kg).

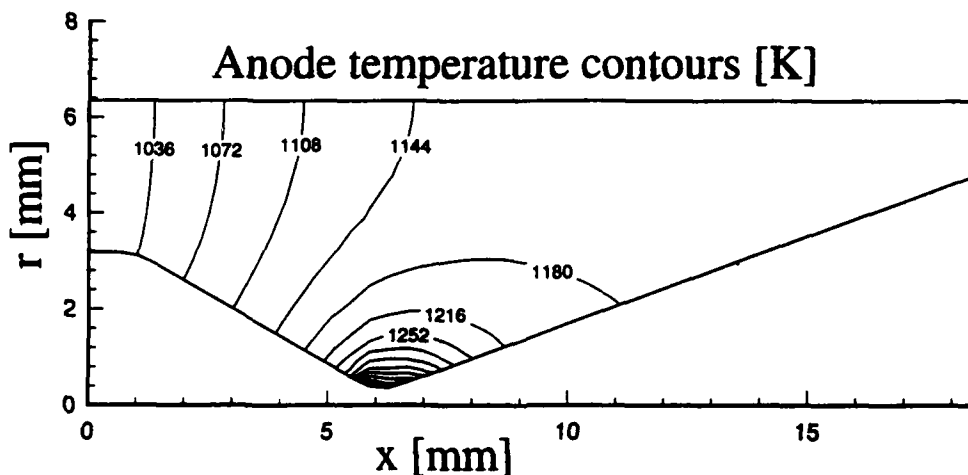


Figure 1-13c: Anode temperature distribution for case 3 ( $N_2H_4$  at  $\frac{P_{\Omega}}{m} = 20$  MJ/kg).

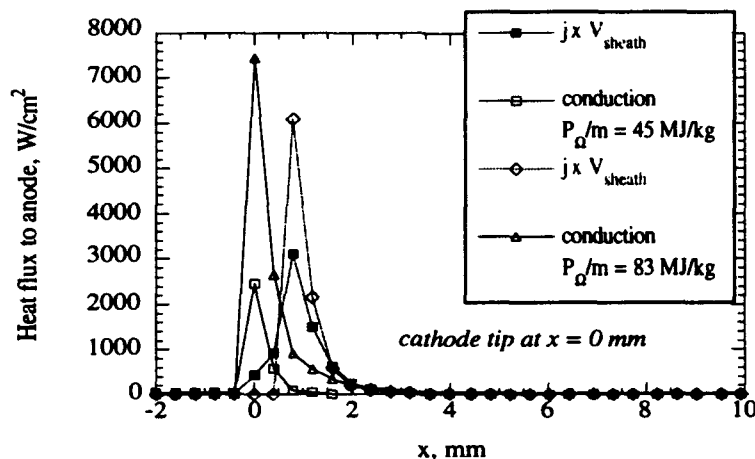


Figure 1-14: Heat losses to the anode for cases 1 and 2.

## 1.5 Conclusions

A two-temperature chemical equilibrium model has been formulated for  $N_2/H_2$  arcjets. A modified set of Navier-Stokes equations employs separate electron and heavy species energy equations to account for separate heavy and electron temperatures. The assumption of chemical equilibrium allows for a tractable solution for the species number densities using the laws of mass action, the plasma equation of state, quasi-neutrality, and species conservation. In this approximation, finite-rate chemistry and diffusion are neglected and the species number densities are determined from the pressure, and electron and heavy temperatures.

Initial non-LTE results indicate that thermal non-equilibrium throughout the arcjet boundary layer significantly reduces the energy transfer from the electrons to the heavy species, and has important implications for the prediction of electrical conductivity. Increasing the specific power deposition reduces the non-equilibrium and improves  $I_{sp}$  but increases the anode thermal loading. The model is capable of producing results for both  $H_2$  and  $N_2H_4$  arcjets. This work represents progress toward a systematic evaluation of the effects of kinetic non-equilibrium on arcjet performance with the goal of providing a useful numerical tool for interpreting experimental results.

## References for Section 1

<sup>1</sup>Wilbur P. J., Jahn, R. G., and Curran, F. C., "Space Electric Propulsion Plasmas," *IEEE Transactions on Plasma Science*, Vol. 19, No. 6, pp. 1167-1179, December, 1991.

<sup>2</sup>Martinez-Sanchez, M., and Sakamoto A., "Simplified Analysis of Arcjet Thrusters," AIAA paper 93-1904, AIAA/SAE/ASME/ASEE 29th Joint Propulsion Conference and Exhibit, June 28-30, 1993, Monterey, Ca.

<sup>3</sup>Rhodes, R. and Keefer, D., "Non-Equilibrium Modeling of Hydrogen Arcjet Thrusters," International Electric Propulsion Conference Paper 93-217, AIAA/ AIDAA/DGLR/JSASS 23rd International Electric Propulsion Conference, September 13-16, 1993, Seattle, Washington.

<sup>4</sup>Miller, S. and Martinez-Sanchez, M., "Nonequilibrium Numerical Simulation of Radiation-Cooled Arcjet Thrusters," International Electric Propulsion Conference Paper 93-218, AIAA/AIDAA/ DGLR/JSASS 23rd International Electric Propulsion Conference, September 13-16, 1993, Seattle, Washington.

<sup>5</sup>Babu, V., Aithal, S., and Subramaniam V. V., "On the Effects of Swirl in Arcjet Thruster Flows," International Electric Propulsion Conference Paper 93-183, AIAA/AIDAA/DGLR/JSASS 23rd International Electric Propulsion Conference, September 13-16, 1993, Seattle, Washington.

<sup>6</sup>Butler, G.W., Kull, A.E., and King, D.Q., "Numerical Simulations of Hydrogen Arcjet Performance," International Electric Propulsion Conference. Paper 93-249, AIAA/AIDAA/ DGLR/JSASS 23rd International Electric Propulsion Conference, September 13-16, 1993, Seattle, Washington.

<sup>7</sup>Flowe, A.C., DeWitt, K.J., Keith, T.G., Jr., Pawlas, G.E., Penko, P.F., "Numerical Modeling of Fluid and Electromagnetic Phenomena in an Arcjet," AIAA Paper 92-3106, AIAA/SAE/ASME/ASEE 28th Joint Propulsion Conference, July 6-8, 1992, Nashville, Tennessee.

<sup>8</sup>Ciucci, A., d'Agostino, L., and Andrenucci, M., "Development of a Numerical Model of the Nozzle Flow in Low Power Arcjet Thrusters," International Electric Propulsion Conference Paper 93-182, AIAA/AIDAA/DGLR/JSASS 23rd International Electric Propulsion Conference, September 13-16, 1993, Seattle, Washington.

<sup>9</sup>Fujita, K. and Arakawa, Y., "Anode Heat Loss and Current Distributions of DC Arcjets," International Electric Propulsion Conference Paper 93-185, AIAA/ AIDAA/DGLR/JSASS 23rd International Electric Propulsion Conference, September 13-16, 1993, Seattle, Washington.

<sup>10</sup>Kruger, C.H., and Mitchner, M., "Kinetic Theory of Two Temperature Plasmas," *Physics of Fluids*, Vol. 10, No. 9, pp. 1953-1961, September 1967.

<sup>11</sup>Krier, H. and Mertogul, A.E., "Two Temperature Modeling and Experimental Measurements of Laser Sustained Hydrogen Plasmas," Annual Technical Report, UILU-ENG 93-4015, Department of Mechanical and Industrial Engineering, University of Illinois at Urbana-Champaign, 1993.

<sup>12</sup>Sutton and Sherman, Engineering Magneto-hydrodynamics, McGraw-Hill, New York, 1965.



<sup>13</sup> Incropera, F. P., and Dewitt, D. P., Fundamentals of Heat and Mass Transfer, John Wiley & Sons, New York, 1981, p 758.

<sup>14</sup> van de Sanden, M. C. M., Schram, P. P. J. M., Peeters, A. G., van der Mullen, J. A. M., and Kroesen, G. M. W., "Thermodynamic Generalization of the Saha Equation for a Two-Temperature Plasma," *Physical Review A*, Vol. 40, No. 9, pp 5273-5276, The American Physical Society, 1989.

<sup>15</sup> Eddy, T. L., Leger, J. M., Coudert, Fauchais P., "Nonequilibrium Diagnostics of a Nitrogen Plasma Jet," HTD-Vol. 161, *Heat Transfer in Thermal Processing*, ASME, 1991.

<sup>16</sup> Fan, W. X. and Dudeck, M. A., "A Study of Concentraions in A Nitrogen Plasma Under Thermal Unbalance Conditions," *J. Chem. Phys.*, Vol. 88, pp 27-37, Elsevier, Paris, 1991.

<sup>17</sup> Drellishak, K. S., Partition Functions and Thermodynamic Properties of High Temperature Gases, Ph.D. Thesis, Northwestern University, 1963.

<sup>18</sup> Stoecker, W. F., Design of Thermal Systems, McGraw-Hill, New York, 1980, pp 117-119.

<sup>19</sup> Capecchi, G. and d'Agostino, L., "Numerical Model of Equilibrium Composition and Transport Coefficients of Hydrazine under Dissociation and Ionization," AIAA Paper 94-2868, 30th AIAA/ASME/SAE/ASEE Joint Propulsion Conference, June 27-29, 1994, Indianapolis, IN.

<sup>20</sup> Mitchner, M., and Kruger, C., Partially Ionized Gases, John Wiley and Sons, New York, 1973.

<sup>21</sup> Maitland, G. C., Rigby, M., Smith, B. E., Wakeham, W. A., Intermolecular Forces, Clarendon Press, Oxford, 1981, p 302.

<sup>22</sup> Stallcop, J. R., Partridge, H., and Levin, E., "Resonance Charge Transfer, Transport Cross Sections, and Collision Integrals for  $N^+(3P)$ - $N(4S^0)$  and  $O+(4S^0)$ - $O(3P)$  Interactions," *J. Chem. Phys.*, Vol. 95, No. 9, pp. 6429-6439, American Institute of Physics, Nov., 1991.

<sup>23</sup> Stallcop, J. R., Bauschlicher, C. W., Partridge, H., and Levin, E., "Theoretical Study of Hydrogen and Nitrogen Interactions: N-H Transport Cross Sections and Collision Integrals," *J. Chem. Phys.*, Vol. 97, No. 8, pp. 5578-5585, American Institute of Physics, Oct., 1992.

<sup>24</sup> Levin, E., Partridge, H., and Stallcop, J. R., "Collision Integrals and High Temperature transport Properties for N-N, O-O, and N-O," *J. Thermophysics*, Vol. 4, No. 4, pp. 469-477, Mitchner Oct. 1990.

<sup>25</sup> Vanderslice, J. T., *et. al*, "High Temperature Transport Properties of Dissociating Hydrogen," *The Physics of Fluids*, Vol. 5, No. 2, pp. 155-164, Feb., 1962.

<sup>26</sup> Stallcop, J. R., Partridge, H., Walch, S. P., and Levin, E., "H-N<sub>2</sub> Interaction Energies, Transport Cross Sections, and Collision Integrals," *J. Chem. Phys.*, Vol. 97, No. 5, pp. 3431-3436, American Institute of Physics, Sept., 1992.

<sup>27</sup> Grier, N. T., "Calculation of Transport Properties of Ionizing Atomic Hydrogen," NASA TN D-1386, National Aeronautics and Space Administration, Washington, D. C., Apr., 1966.

<sup>28</sup>Chang, C. H. and Pfender, E., "Nonequilibrium Modeling of Low Pressure Argon Plasma Jets; Part I: Laminar Flow," *Plasma Chemistry and Plasma Processing*, Vol. 10, No. 3, pp. 473-491, 1990.

<sup>29</sup>Burton, R. L., Bufton, S. A., Tiliakos, N. T., and Krier, H., "Application of Multiple Electrostatic Probes to a Low Power Arcjet," AIAA Paper 94-3299, to be presented at the AIAA 30th Joint Propulsion Conference, June 27-29, 1994, Indianapolis, IN, 1994.

<sup>30</sup>Issa, R. I., "Solution of the Implicitly Discretised Fluid Flow Equations by Operator-Splitting," *Journal of Computational Physics*, Vol. 62, pp. 40-65, 1986.

<sup>31</sup>Rhie, C. M., "A Pressure-Based Navier Stokes Solver Using The Multigrid Method," AIAA Paper 86-0207, AIAA 24th Aerospace Sciences Meeting, Jan. 6-9, Reno, Nevada, 1986.

<sup>32</sup>Karki, K.C., A Calculation Procedure for Viscous Flows at All Speeds in Complex Geometries, Ph.D. Thesis, University of Minnesota, 1986.

<sup>33</sup>Megli, T. W., Krier, H., Burton, R. L., and Mertogul, A. E., "Two Temperature Modeling of N<sub>2</sub>/H<sub>2</sub> Arcjets," AIAA Paper 94-2413, 25th AIAA Plasmadynamics and Lasers Conference, June 20-23, 1994, Colorado Springs, CO.

## Section 2: Exit Plane Electrostatic Probe Studies\*

### 2.1 Quadruple Probe Experiments

#### Introduction

The use of electrostatic probes has long been an attractive method for experimentally determining plasma parameters in both laboratory and space plasmas. Recently, several authors<sup>1-4</sup> have employed classical Langmuir<sup>5</sup> (single) probes in the characterization of low power arcjet plumes. While single probes are relatively simple to construct, it is necessary to sweep the bias voltage supplied to the probe while measuring the V-I characteristic. In addition, it is a significant effort to extract the electron density  $n_e$  and electron temperature  $T_e$  from the corresponding V-I characteristic. Alternatively, a triple probe system<sup>6</sup> can be employed which allows simultaneous measurement of  $T_e$  and  $n_e$  without the necessity of a voltage sweep. The feasibility of applying triple probes to electric propulsion devices has been demonstrated in MPD thruster plumes<sup>7</sup> and, more recently, in low power arcjet plumes.<sup>8</sup> In addition, Habiger, *et al.*<sup>9</sup> have recently presented a general review of electrostatic probe techniques and their uses in electric propulsion devices.

Using the theory developed originally by Kanal,<sup>10</sup> several authors have measured velocities in flowing plasmas using a crossed-probe technique.<sup>11, 12</sup> By combining the crossed-probe method and the triple probe technique discussed above, a quadruple electrostatic probe has been devised and its use demonstrated in an MPD thruster.<sup>13, 14</sup> The quadruple probe is capable of simultaneously yielding  $T_e$ ,  $n_e$ , and the ratio of the plasma velocity to the most probable thermal speed ( $u_i/c_m$ ). The goal of the present research is to demonstrate the usefulness of the quadruple probe in the near-field plume, less than 1.5 mm from the thruster exit plane, of a low power arcjet thruster.

#### Quadruple Probe Schematic and Potential Plot

Figures 2.1a and 2.1b show an electrical schematic and potential plot of the quadruple probe, consisting of three cylindrical probes  $P_1$ ,  $P_2$ ,  $P_3$  which are aligned with the plasma flow vector and one probe  $P_4$  which is perpendicular to the plasma flow.  $P_3$  and  $P_4$  are biased at constant voltages  $V_{d3}$  and  $V_{d4}$  relative to  $P_1$ , and  $P_2$  assumes the floating potential  $V_f$  of the local plasma ( $I_2=0$ ). Probes 1, 3 and 4 are also electrically floating so that ion current collected by  $P_3$  and  $P_4$  is balanced by the electron current collected by  $P_1$ . Three quantities are recorded: currents  $I_3$  and  $I_4$  and the potential difference  $V_{d2}$ .

---

\*Ph.D. Candidate, Scott A. Bufton, leads our group in advanced probing in the exit plane of a 1 kW class arcjet.

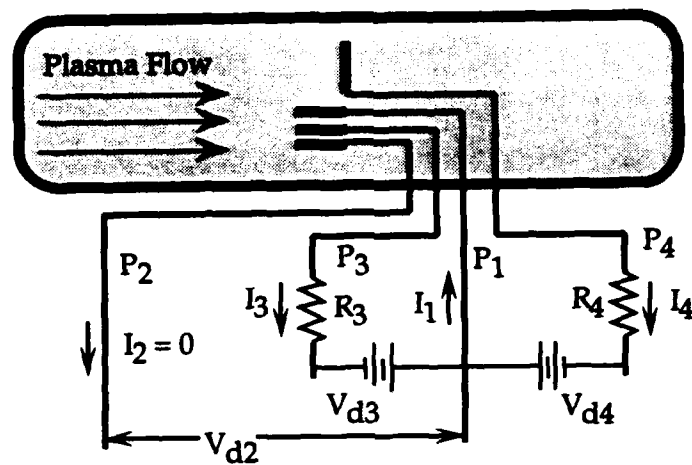


Fig. 2.1a. Quadruple probe electrical schematic

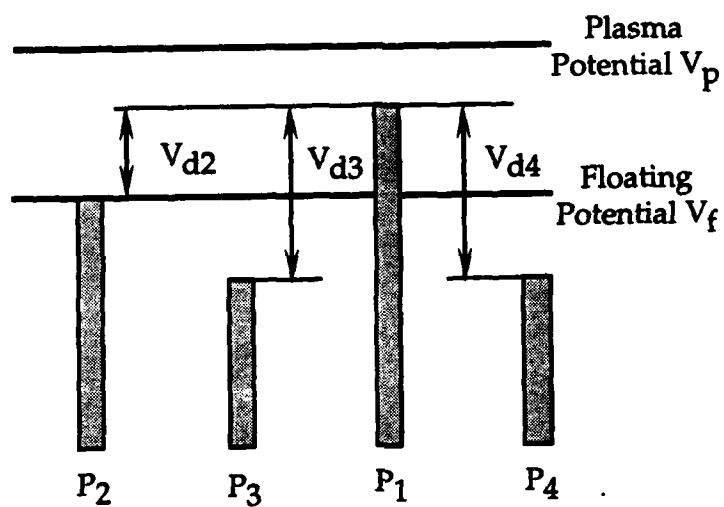


Fig. 2.1b. Quadruple probe potential plot for constant plasma potential  $V_p$ .

The addition of the perpendicular probe  $P_4$  allows the determination of the parameter  $u_i/c_m$ , determined from the ratio  $I_4/I_3$  for crossed probes with  $V_{d3} = V_{d4}$ . Currents  $I_3$  and  $I_4$  are determined by measuring voltage drops across resistors. In Fig. 2.1, voltages  $V_{d3}$  and  $V_{d4}$  are provided by batteries, with  $V_{d3}=V_{d4}=12V$ .

### Quadruple Probe Theory

Quadruple probe analysis assumes: 1) The ion sheath surrounding the tungsten electrodes is thin compared to the wire radius  $r_p$ ; 2) Each probe wire and sheath are collisionless ( $\lambda_{mfp} \gg r_p \gg$  sheath thickness); 3) The electron energy distribution is Maxwellian; and 4) A wake region of low ion and electron density downstream of  $P_4$  generates collection areas for ions and electrons of  $A_{4i}=A/\pi$  and  $A_{4e}=A/2$ , respectively.

Derivation of quadruple probe response is similar to that of the triple probe<sup>6</sup> and has been presented elsewhere.<sup>13,14</sup> In the present study, the probe is applied to a simulated hydrazine plume, with multiple species of ions present, whereas previous applications of triple and quadruple probes have been for plasmas with one dominant species of positive ion. Single Langmuir probes have been used in nitrogen and hydrogen-based arcjet plumes,<sup>1-4</sup> but their use is not contingent on knowledge of the species.

For a quadruple probe with  $A_1=A_2=A_3=A$ ,  $A_{4i}=A/\pi$ ,  $A_{4e}=A/2$  and  $V_{d3}=V_{d4}$ , the following expression can be derived:

$$1 = \frac{1 + \exp(\phi V_{d3}) - 2 \exp[\phi (V_{d3} - V_{d2})]}{\left\{ \frac{1}{\pi} \exp[\phi (V_{d3} - V_{d2})] - \frac{1}{2} \right\}} \quad (2.1)$$

Since  $V_{d3}$  is prescribed and  $V_{d2}$  is experimentally determined, Eq. 2.1 determines  $T_e = e/k\phi$  through iteration. Knowledge of the plume species is not required to determine electron temperature.

The ion saturation current density  $j_i$  is related to measured quantities by

$$j_i = \frac{3 I_3}{2A \left[ \exp(\phi V_{d2}) - \left( \frac{1}{2} + \frac{1}{\pi} \right) \right]} \quad (2.2)$$

Normally, Eq. 2.2 is used to determine  $n_e$  from  $I_3$  and  $V_{d2}$  by relating  $j_i$  to the electron density through the Bohm sheath analysis. For a plasma with only one species of positive ion, the Bohm analysis gives

$$j_i = e n_e \left( \frac{kT_e}{m_i} \right)^{1/2} \exp \left( -\frac{1}{2} \right) \quad (2.3)$$

For a plasma with multiple ion species Eq. 2.3 must be modified. Assuming that each collected positive ion behaves independently as it accelerates through the Bohm sheath toward the probe,  $j_i$  becomes:

$$j_i = e (kT_e)^{1/2} \exp \left( -\frac{1}{2} \right) \left[ \sum_{j=1}^{\text{\# species}} \left( \frac{n_j}{(m_j)^{1/2}} \right) \right] \quad (2.4)$$

Assuming equilibrium dissociation of  $2H_2 + N_2$  in the arcjet constrictor with each species concentration frozen between the constrictor and the exit plane, numerical equilibrium codes predict  $H^+$  and  $N^+$  as the only positive ions present in measurable levels,<sup>15</sup> with  $0.4 < n_{N^+}/n_{H^+} < 0.7$  for most equilibrium temperatures of interest (Fig. 2.2). The Bohm ion saturation current is then:

$$j_i = e (kT_e)^{1/2} \exp \left( -\frac{1}{2} \right) \left( \frac{n_{H^+}}{(m_{H^+})^{1/2}} + \frac{n_{N^+}}{(m_{N^+})^{1/2}} \right) \quad (2.5)$$

For  $n_e = n_{H^+} + n_{N^+}$ , Eqs. 2.2 and 2.5 yield

$$n_e = \frac{\kappa (3 I_3 \exp(1/2) (m_{H^+})^{1/2})}{2 A e (kT_e)^{1/2} \left[ \exp(\phi V_{d2}) - \left( \frac{1}{2} + \frac{1}{\pi} \right) \right]} \quad (2.6)$$

where  $\kappa$  is the correction to the electron density due to multiple ion species:

$$\kappa = \frac{1 + \left( \frac{n_{N^+}}{n_{H^+}} \right)}{1 + \left( \frac{n_{N^+}}{n_{H^+}} \right) \left( \frac{m_{H^+}}{m_{N^+}} \right)^{1/2}} \quad (2.7)$$

Note that Eq. 2.6 neglects velocity slip between each species of ion and radial diffusion of  $H^+$  and  $N^+$ . For a plume containing only  $H^+$ ,  $n_{N^+} = 0.0$ ,  $\kappa$  reduces to unity, and Eq. 2.6 reduces to single component form. Figure 2.3 gives  $\kappa$  as a function of the ion number density ratio for an H-N plasma. For  $6,000 < T < 20,000$  K, Figs. 2.2 and 2.3 predict  $1 < \kappa < 1.4$ .

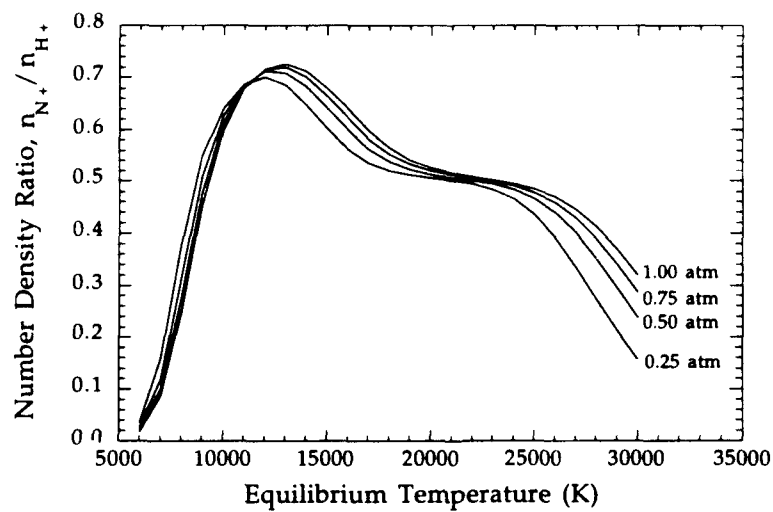


Fig. 2.2. Equilibrium  $N^+/H^+$  density ratio.

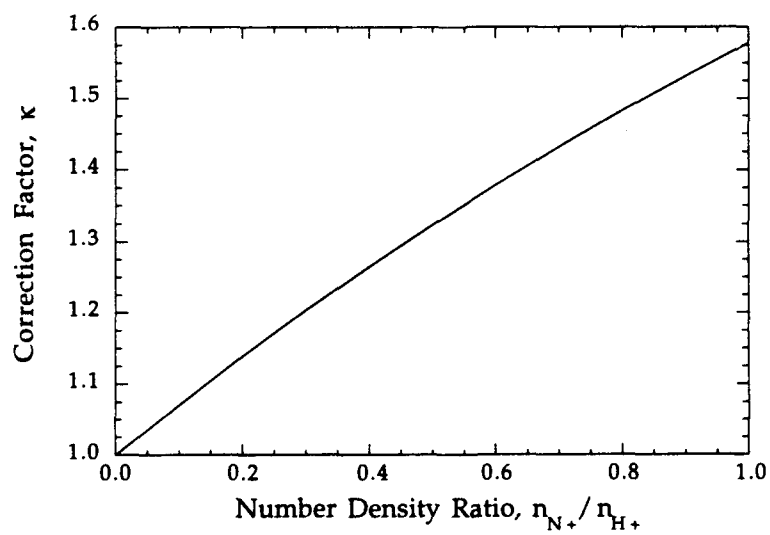


Fig. 2.3. Correction factor for electron density  $n_e$  in an H-N plasma due to  $N^+$  ions.

The use of crossed electrostatic probes for measuring plasma velocity<sup>10,12</sup> and the implementation of the crossed probe technique into the quadruple probe<sup>13,14</sup> have been presented elsewhere. For a cylindrical electrode oriented at an angle  $\theta$  relative to the plasma flow, the collected ion current is a function of the quantity  $(u_i/c_m)\sin\theta$ . For the case of two equally biased probes, with one probe aligned with the flow vector and the other one normal to it, the single species collected ion current ratio is:<sup>12</sup>

$$\frac{I_{\perp}}{I_{\parallel}} = \frac{I_4}{I_3} = \frac{2A_4}{\sqrt{\pi} A_3} \exp(u_i/c_m)^2 \sum_{n=0}^{\infty} \left[ \frac{(u_i/c_m)^n}{n!} \right]^2 \Gamma\left(n + \frac{3}{2}\right) \quad (2.8)$$

Because of the wake effect described above, the current collection area ratio for ions is  $A_4/A_3 = 1/\pi$ . Combining Eq. 2.8 with measurements of the currents  $I_3$  and  $I_4$  yields the quantity  $u_i/c_m$ , which is related to the plasma Mach number by  $M = (2/\gamma)^{1/2}(u_i/c_m)$ , where  $\gamma$  is the specific heat ratio of the plasma. If information about the ion temperature  $T_i$  is known ( $c_m = (2kT_i/m_i)^{1/2}$ ) the plasma streaming velocity can be determined from Eq. 2.8.

### Apparatus / Experimental Approach

Electrostatic probe experiments were carried out at the exit plane of a 1 kW NASA arcjet thruster<sup>16</sup> operating at a flow rate of 50 mg/s of  $2H_2 + N_2$  to simulate fully decomposed hydrazine. Each component of the propellant was individually metered by Unit mass flow controllers and mixed in the propellant line. The thruster operated at 10 A and 104 to 110 volts, depending on how long the arcjet had been operating, and exhausted into a 1 m diameter x 1.5 m long vacuum tank pumped by a 2500 cfm Roots-type blower. Backing for this was provided by a second 1300 cfm Roots blower and two 150 cfm displacement pumps. The tank pressure during arcjet operation was ~200 mTorr.

A schematic of the quadruple probe utilized in this study is shown in Fig. 2.4. The probe is comprised of 4 individual tungsten wire tips of 0.25 mm diameter with an exposed length of 3.5 mm. Each wire mounts in round four-bore alumina ( $Al_2O_3$ ) tubing, providing rigidity, electrical insulation, and high heat capacity to allow probe measurements at the exit plane of the thruster. The alumina is 2.4 mm in diameter, with four 0.5 mm diameter through holes (Fig. 2.4), and is mounted in thin-walled stainless steel tubing to provide noise shielding and to facilitate mounting the probe and its leads to the positioning mechanism. In early experiments, epoxy was used to secure each wire in the alumina, but the epoxy tended to ablate away over time, exposing more of each tungsten electrode. This method was abandoned in favor of a high temperature ceramic-based adhesive to bond each wire to the alumina.



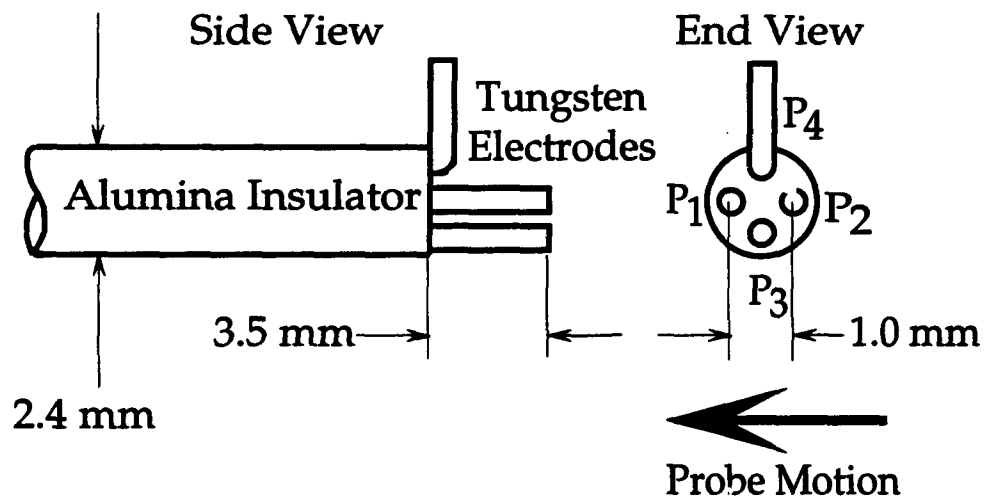


Fig. 2.4. Schematic of quadruple probe tip swept through the arcjet plume.

The thin-wall stainless steel tube is rigidly connected to two ceramic thermocouple plugs with a compression fitting (Fig. 2.5). Each plug houses connections for two tungsten wires, allowing connection to the probe electronics by a single four-prong plug located at the rear and a vacuum feedthrough in the tank wall.

The complete assembly is mounted to a stepper motor mounted on a linear translation carriage (Fig. 2.5). The stepper motor allows the probe axis to be rotated in increments of  $0.9^\circ$ . The probe arm is coupled directly to the motor shaft with the probe sensing tip on the shaft axis, allowing probe angle to be varied without changing the tip location. For the present study, the probe axis is always parallel to the thruster axis.

The motor and probe assembly is mounted to a carriage capable of a  $\pm 5$  cm linear translation perpendicular to the arcjet axis, allowing the quadruple probe assembly to be manually swept through the plume. The carriage platform is mounted to a precision shaft/linear ball bearing assembly giving smooth and repeatable probe movement by a shaft passing through a vacuum feedthrough in the tank wall. Carriage and probe position are determined by a precision  $10\text{ k}\Omega$  linear potentiometer coupled to the carriage shaft. The probe position is determined to  $0.05\text{ mm}$  relative to the arcjet nozzle by calibrating the  $10\text{ k}\Omega$  linear potentiometer output against the outer diameter of the nozzle. The probe system can be removed as a unit from the vacuum system and bench-tested.

### Quadruple Probe Preliminary Results and Analysis

Preliminary experimental results are presented for the near-field plume of the thruster, with the probe tip located  $1.5\text{ mm}$  from the thruster exit. Electron densities are calculated using Eq. 2.6, with a correction factor  $\kappa=1.35$ , which corresponds to  $n_{N^+}/n_{H^+}=0.55$ . Variation of  $0.4 < n_{N^+}/n_{H^+} < 0.7$  causes only a  $\pm 5\%$  error in  $\kappa$  and, hence, in  $n_e$ . Electron number density results are shown in Fig. 2.6 for probe sweeps recorded at  $\sim 4$  minute intervals during arcjet warm-up. Low  $n_e$  is measured by the probe outside of the exit plane diameter, as expected. The electron temperature used to determine  $n_e$  is  $1\text{ eV}$  for each case, as discussed below. For the range  $0.3 < T_e < 1.0$  expected at the exit plane,  $n_e$  varies approximately as  $T_e^{-1/2}$ , so that a corresponding correction to the  $n_e$  values of Fig. 2.6 must be made. The increases in  $n_e$  with time in Fig. 2.6 are not due to variations in  $T_e$ , since a factor of 3 decrease in  $T_e$  would be required to explain the measured increase in  $n_e$ .

The thruster appears to be operating in a steady state condition, based on probe measurements, after approximately 4 to 8 minutes. This is consistent with previously reported

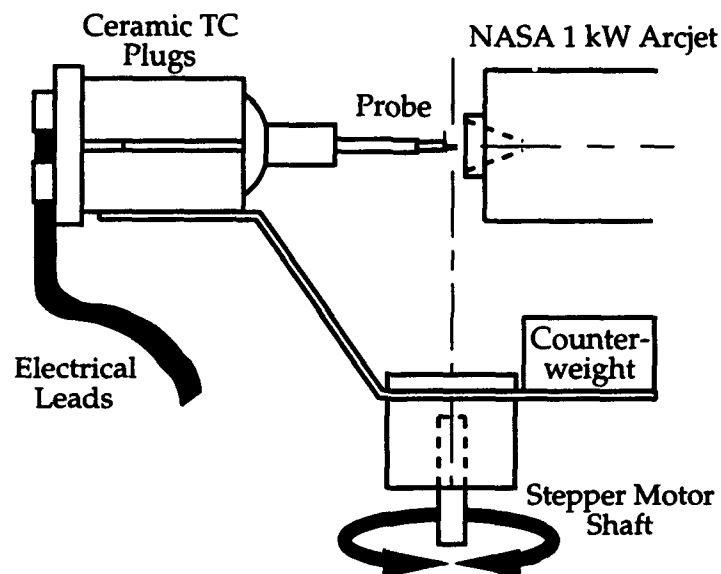


Fig. 2.5. Schematic of quadruple probe mount. Probe axis is parallel to the thruster in this study.

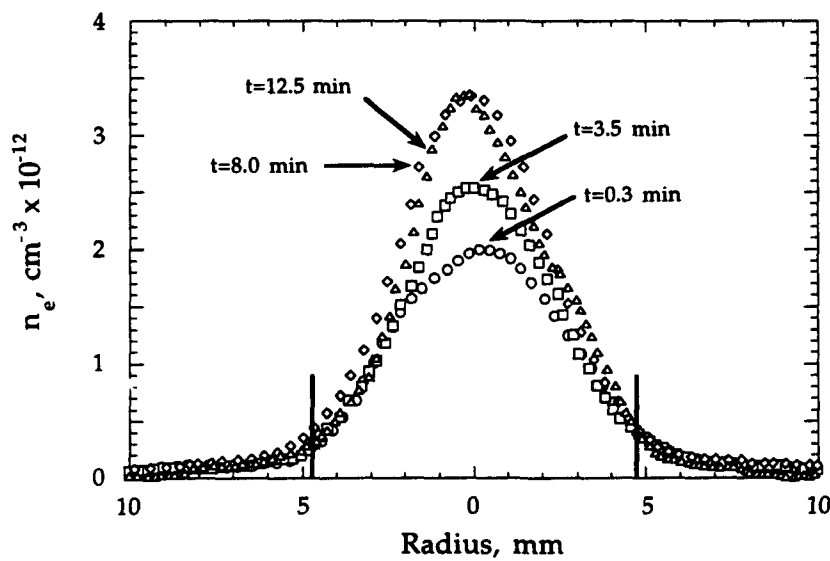


Fig. 2.6. Electron density  $n_e$  versus radius during thruster warm-up.

data indicating that the arcjet operating voltage level is 98% of its steady state level after approximately 5 minutes of operation.<sup>16</sup>

Since the quadruple probe is aligned with the thruster axis during these sweeps, a correction is required to account for the effect of flow transverse to the probe axis. For probe locations near the plume centerline, these corrections are small. At locations far from the thruster axis this correction may be quite large, but the thin sheath assumption breaks down in these regions and a correction was not attempted. Assuming a correction to the  $n_e$  values in Fig. 2.6 consistent with a centerline  $T_e$  of 0.5 eV, our data are lower than the  $n_e$  results of other researchers<sup>17</sup> by a factor of  $\sim 2 - 4$ .

The measured currents  $I_3$  and  $I_4$  and the current ratio  $I_4/I_3$  used to determine  $u_i/c_m$  from Eq. 2.8 are plotted in Fig. 2.7 for  $t \sim 8$  minutes after arcjet start-up. For  $r < 3$  mm near the centerline,  $I_4/I_3 \sim 0.6$ , corresponding to  $u_i/c_m = 1.5$  and a Mach number  $M \sim 1.9$ . This calculation neglects the effect of multiple species on the ion current to the crossed probes. For dissociated hydrazine at 0.5 eV, with a mean molecular weight of 5.3, the sound speed is a  $\sim 3,300$  m/s, and the corresponding  $M = 1.9$  flow velocity is 6,200 m/s. This low Mach number is consistent with results for high area ratio, low Reynolds number nozzles.

A typical  $V_{d2}$  trace versus position across the thruster face is shown in Fig. 2.8. Since, by Eq. 2.1,  $T_e$  increases monotonically with  $V_{d2}$ , the non-symmetric  $V_{d2}$  trace would seem to imply the unexpected result of non-symmetric  $T_e$ , with  $T_e$  increasing monotonically from a minimum of  $\sim 0.5$  eV at  $r = 3$  mm to  $\sim 0.7$  eV on axis to  $\sim 1.2$  eV at the right side of the exit plane. Because of the symmetry in the  $n_e$  profiles, this amount of  $T_e$  asymmetry seems unlikely.

Several experiments were performed to investigate the nature of the observed  $V_{d2}$  asymmetry. Probe heating and thermionic emission of electrons were first eliminated by examining  $V_{d2}$  traces obtained by passing the probe through the plume in each of two possible directions. The resulting traces in this case were mirror images of each other, indicating that probe heating was not a factor. To rule out physical asymmetry in the plume, the entire thruster was rotated  $180^\circ$  about the thrust axis. This experiment yielded results identical to those recorded before the arcjet was rotated.

Probe asymmetry itself was then investigated. Initial experiments were conducted with a quadruple probe configured as shown in Fig. 2.9a. A more symmetric configuration, Fig. 2.9b, showed improvement but not elimination of the asymmetry.

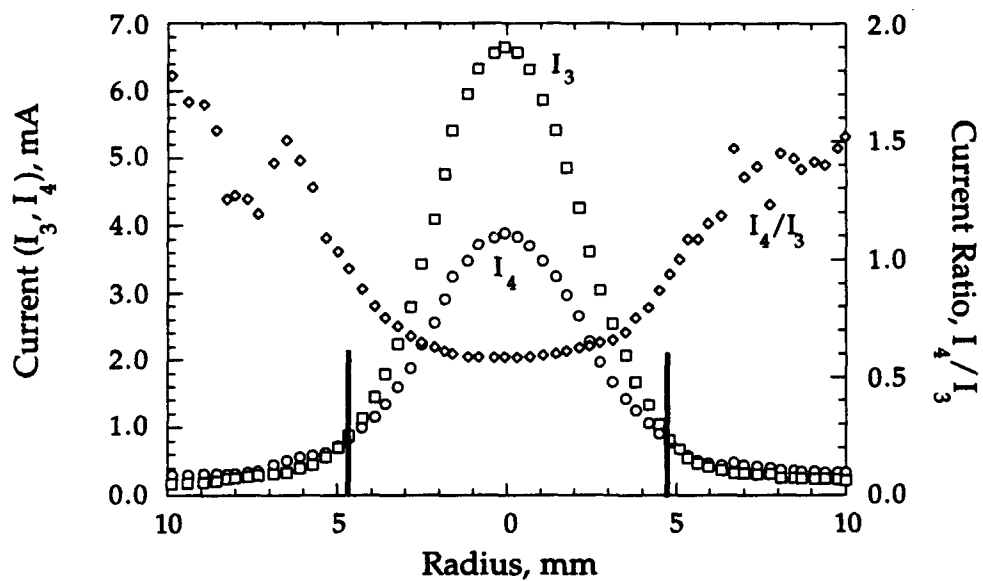


Fig. 2.7. Probe currents  $I_3$ ,  $I_4$ , and  $I_4/I_3$  giving  $M \sim 1.9$  in the center of the plume.

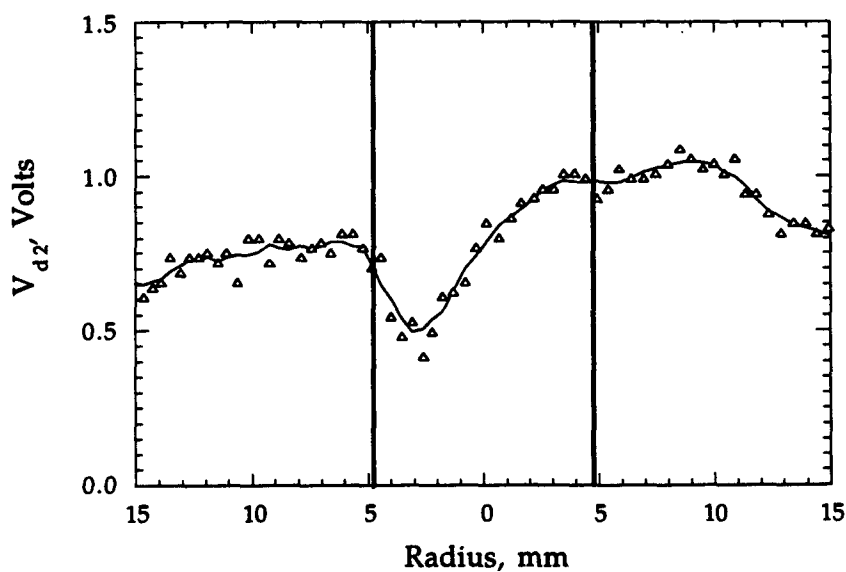


Fig. 2.8. Typical  $V_{d2}$  vs.  $r$  showing asymmetry due to  $V_p$  gradients, and  $T_e \sim 0.6$  eV on axis.

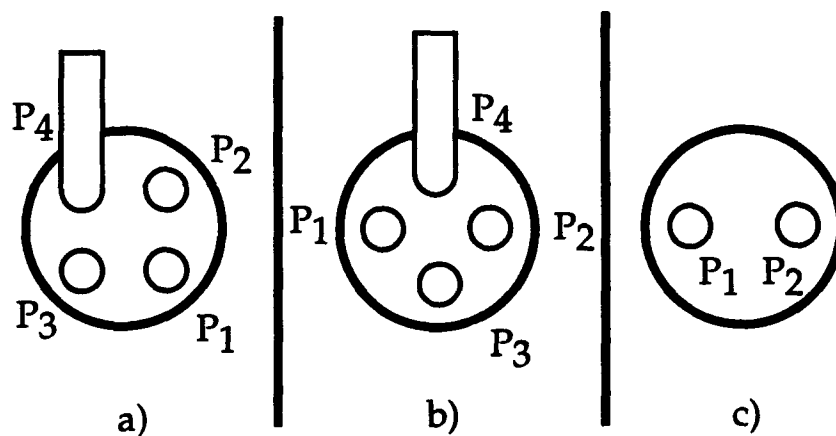


Fig. 2.9. Quadrupole probe configurations used to change probe symmetry (a, b) and for radial E-field measurements (c).

It thus appears likely that radial gradients in the plasma parameters ( $T_e$ ,  $n_e$ ,  $V_p$ ) across the probe volume cause the asymmetry. To verify this, the double floating probe configuration shown in Fig. 2.9c was used to measure the radial electric field  $E_r$ . For two floating probes in a plasma with sheath potential  $V_s$  and a potential difference between the two electrodes  $\Delta V_f = V_{f2} - V_{f1}$ , the difference in plasma potential is:

$$V_{p2} - V_{p1} = V_{f2} - V_{f1} - (V_{s2} - V_{s1}) \quad (2.9)$$

The results of a  $\Delta V_f$  measurement are plotted in Fig. 2.10. The difference in sign between the two peaks at  $r=5.5$  mm is a consequence of electrode orientation remaining constant while the plasma gradients change sign from one side of the plasma plume to the other. From Eq. 2.9, the change in plasma potential across the probe can be found if  $\Delta V_f$  and the probe sheath drops are known. For a single floating electrode, the sheath potential drop  $V_s$  is given in the usual way by summing the ion and electron current into the probe and solving for the potential in the Boltzmann term that satisfies the zero net current requirement. This yields a sheath potential of

$$V_s = \frac{kT_e}{2e} \ln \left( \frac{m_i T_e}{m_e T_i} \right) \quad (2.10)$$

Assuming that the logarithm term does not vary much over the probe separation,

$$V_{s2} - V_{s1} = \Delta V_s \approx \frac{k}{2e} \Delta T_e \ln \left( \frac{m_i T_e}{m_e T_i} \right) \quad (2.11)$$

If we assume that the gradients in electron temperature are small over the electrode separation, then  $\Delta V_s = 0$  and measurements of  $\Delta V_f$  will equal the plasma potential difference  $V_{p2} - V_{p1}$ , and radial electric field  $E_r = \Delta V_f / d$  at the thruster exit. The resulting magnitude of  $E_r$  versus position is shown in Fig. 2.11. The field is approximately zero at the center as expected, with peaks of  $\sim 200$  V/m near the edges of the thruster exit plane. From  $E_r = -dV_p/dr$ , we can integrate the electric field to give the profile of  $V_p$  across the thruster exit (Fig. 2.12) showing a plasma potential profile with a shallow potential well of depth  $\sim 0.1$  V, with its minimum near the thruster axis and steep gradients outside the exit plane at  $r > 5$  mm.

The probe measurements are strong evidence for the existence of current density and ohmic heating in the near-field plume. From the mass flow rate and measured  $n_e$ , the estimated ionization fraction on the centerline is  $\alpha \approx 10^{-4}$ , giving a plasma electrical conductivity of  $\sigma \approx 100$  mho/m. In the exit plane  $E_r \sim 100$  V/m, equivalent to  $j = \sigma E \sim 1$  A/cm<sup>2</sup> crossing the exit plane of

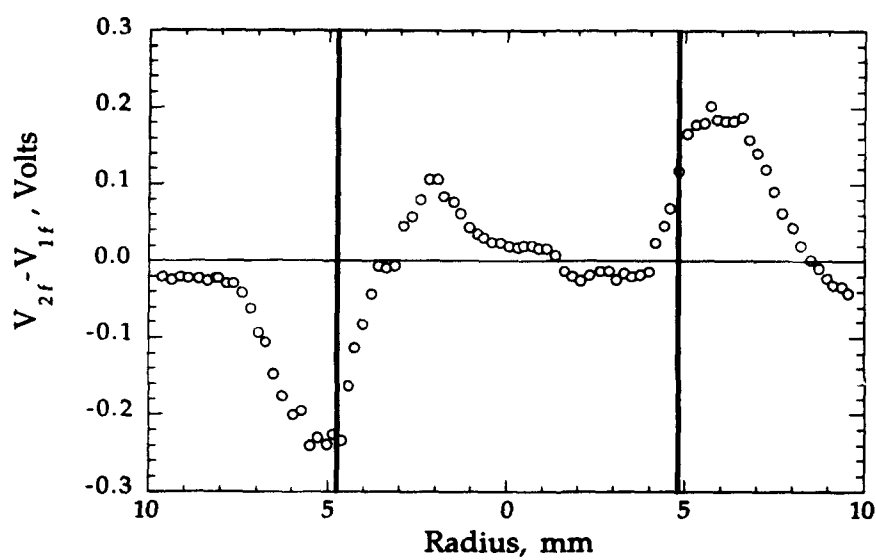


Fig. 2.10.  $V_{2f} - V_{1f}$  measurement with E-field configuration.

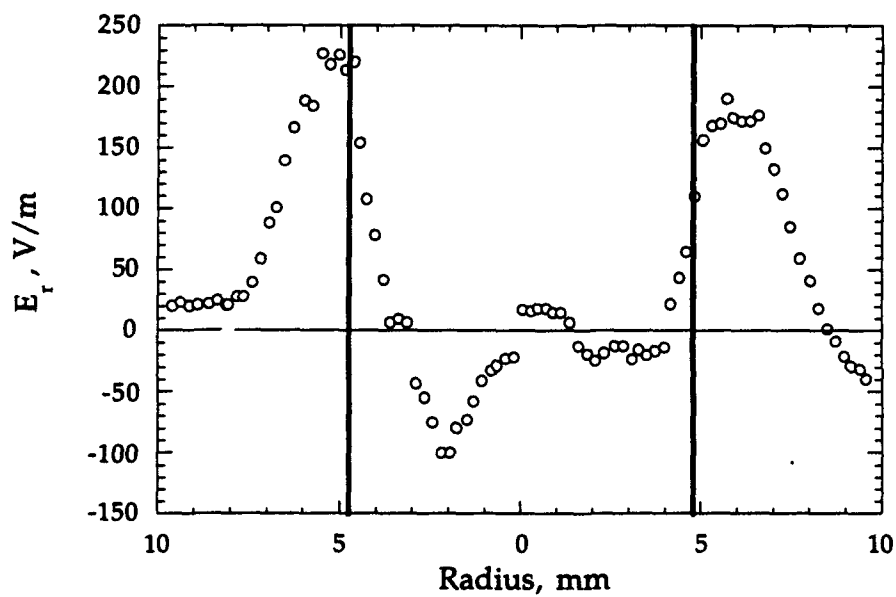


Fig. 2.11. Radial E-field versus position across thruster face.



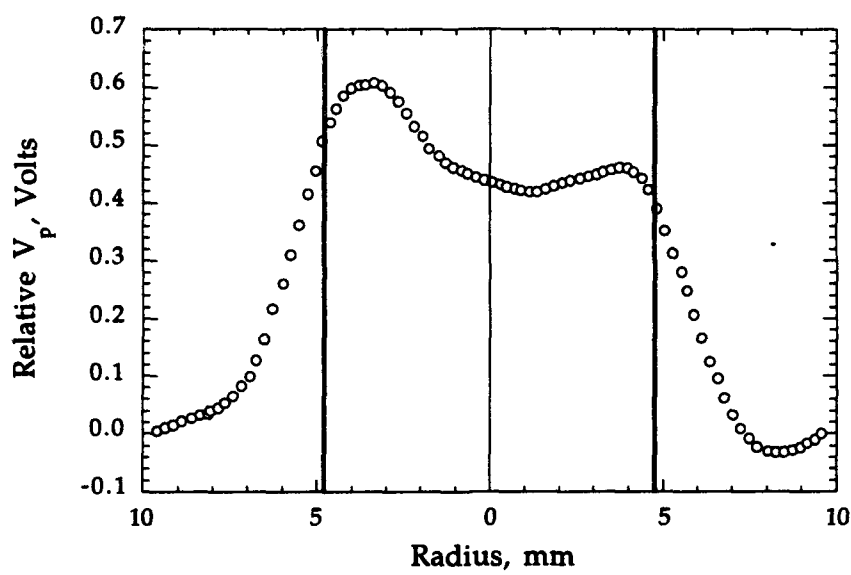


Fig. 2.12. Voltage potential obtained by integrating the radial E-field data.

the thruster and reattaching at the corner of the nozzle. If this current is flowing into a region of approximately  $0.2 \text{ cm}^2$ , the total current crossing the exit plane amounts to  $\sim 0.2 \text{ A}$ , or 2% of the total current supplied to the arcjet. Furthermore, this current represents a small amount of ohmic heating ( $j^2/\sigma \sim 1 \text{ W/cm}^3$ ) in the exit plane region.

The indication seen here of current in the near-field plume is consistent with the condition of  $j$  perpendicular to the nozzle wall, which would force current into the plume. These preliminary measurements also may carry implications for choosing downstream boundary conditions for arcjet numerical models.

### Implications of Non-uniform Plasma Potential

The basic triple and quadruple probe theories<sup>6,14</sup> assume zero  $\Delta V_p$ , strictly true here only on axis. Figure 2.13 is a potential plot for the quadruple probe in a plasma potential gradient (E-field). Because biasing voltages  $V_{d3}$  and  $V_{d4}$  are large, small changes in  $V_p$  have little effect on the ion saturation current. However, the gradient in  $V_p$  can affect the measured  $T_e$ . It can be shown that the quadruple probe (qp) voltage  $V_{d2}$  (Fig. 2.13) is given more generally by:

$$V_{d2} = |V_{2m} - V_{1m}|_{qp} - (V_{p2} - V_{p1}) \quad (2.12)$$

Substituting for  $V_{p2} - V_{p1}$ , as measured by a double floating probe (dfp), from Eq. 2.9:

$$V_{d2} = |V_{2m} - V_{1m}|_{qp} - [(V_{f2} - V_{f1})_{dfp} - (V_{s2} - V_{s1})_{dfp}] \quad (2.13)$$

Combining Eqs. 2.11 and 2.13, the electron temperature can, in principle, be determined despite the existence of gradients in  $V_p$ . This work is in progress.

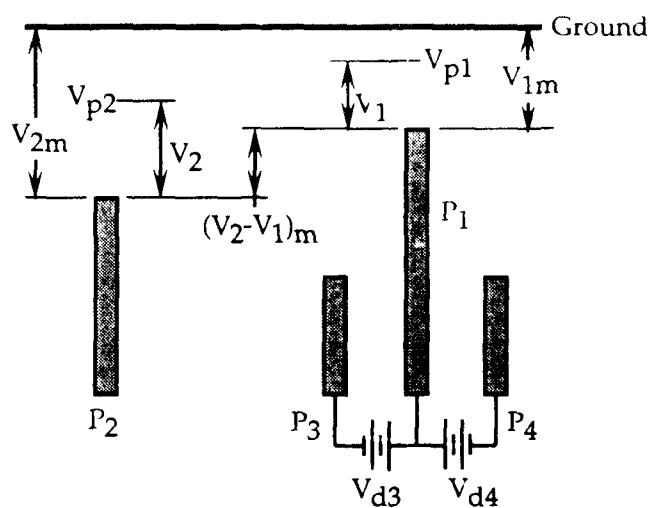


Fig. 2.13. Potential plot for the quadrupole probe in a plasma potential gradient (E-field), where  $V_{p1} \neq V_{p2}$ .

## 2.2 Quadruple Probe Modeling with Plasma Gradients

### Introduction

Preliminary results of quadruple probe measurements at the thruster exit plane show smooth symmetric profiles for  $n_e$  (Fig. 2.6) and the electrode currents  $I_3$  and  $I_4$  (Fig. 2.7). However, Fig. 2.8 shows an asymmetric  $V_{d2}$  profile, which directly implies an unexpected asymmetry in the measured  $T_e$  profile through Eq. 2.1. Several possible explanations for this asymmetry have been considered, including: 1) electrode heating and thermionic emission, 2) the presence of a physical asymmetry in the plume, 3) probe geometry, and 4) the influence of gradients in plasma parameters over the probe volume. Each of the first three reasons were eliminated as possibilities through a judicious choice of experiments, leaving the fourth explanation as a remaining possibility.

The quadruple probe theory derived in Section 2.1 assumes that the various plasma parameters ( $T_e$ ,  $n_e$  and  $V_p$ ) are uniform over the probe volume. It has been hypothesized, despite the small ( $\sim 1$  mm) width of the quadruple probe, that slight gradients in the plasma parameters over the probe volume may be responsible for the asymmetric  $T_e$  profiles measured at the exit plane. This possibility is being investigated by examining the effect of selected radial profiles of  $T_e$  and  $n_e$  on the quadruple probe results when the current to each electrode is evaluated at the local  $T_e$  and  $n_e$  of each electrode. More precisely, a quadruple probe computational model has been constructed that effectively runs the quadruple probe experiment in reverse. In this way, one can specify profiles of  $T_e$  and  $n_e$  and calculate the quantities normally measured by the quadruple probe: the difference in the potentials of electrodes 1 and 2 ( $V_{d2}$ ); and the measured current drawn by electrode 3 ( $I_3$ ). The predicted values of  $V_{d2}$  and  $I_3$  can then be compared to the corresponding measured values to gain insight into the extent that the finite dimensions of the electrostatic probe influence the measured profiles of  $T_e$  and  $n_e$ . Ultimately, the model may provide a means of solving for the  $T_e$  and  $n_e$  profiles from the measured asymmetry in the  $V_{d2}$  signal.

### Model Derivation

In the laboratory, the measured quadruple probe parameters  $V_{d2}$  and  $I_3$  are related to  $T_e$  and  $n_e$  through Eqs. 2.1 and 2.6. To develop the quadruple probe model in the presence of plasma gradients, the four individual electrode current equations are rewritten in terms of the plasma parameters near each electrode, instead of assuming uniformity in  $T_e$  and  $n_e$  across the probe volume. The electrode current equations are rearranged to solve explicitly for  $V_{d2}$  and  $I_3$  in terms of specified profiles of  $T_e$  and  $n_e$ . This results in the following relations for the performance of the quadruple probe:

$$V_2 = V_2(T_{e2}, n_{e2}) \quad (2.14)$$

$$V_1 = V_1(T_{e1}, T_{e3}, T_{e4}, n_{e1}, n_{e3}, n_{e4}) \quad (2.15)$$

$$V_{d2} = V_2 - V_1 \quad (2.16)$$

$$I_3 = I_3(T_{e3}, n_{e3}) \quad (2.17)$$

The subscripts on the parameters  $T_e$  and  $n_e$  in the above equations denote the local value of those parameters at each of the four electrodes (1-4) making up the quadruple probe.

Initial versions of this model have been implemented in a spreadsheet format that solves for  $V_{d2}(r)$  and  $I_3(r)$ , for given profiles of  $T_e(r)$  and  $n_e(r)$ . Since the centerline experimental data are, by symmetry, at zero gradient conditions, these data are used to determine the centerline values of  $T_e$  and  $n_e$ . For the initial version of the model,  $T_e(r)$  and  $n_e(r)$  are specified as Gaussian distributions, with a peak value corresponding to the experimentally measured thruster centerline values. The width (standard deviation) of each profile is adjusted to study the effect on the predicted quantities  $V_{d2}$  and  $I_3$ . Since  $V_{d2}$  (Eq. 2.16) and  $I_3$  (Eq. 2.17) are strong functions of  $T_e$  and  $n_e$ , respectively, there is sufficient uncoupling that the model can be used to solve iteratively for the  $T_e(r)$  and  $n_e(r)$  profiles to reproduce the measured  $V_{d2}$  and  $I_3$  profiles. The numerical program moves the probe position across the thruster face in  $\sim 0.1$  mm increments ( $\sim 1/10$  of the probe width) while solving for the predicted values  $V_{d2}$  and  $I_3$ , which are then compared to the measured values  $V_{d2}$  and  $I_3$ . The  $T_e$  and  $n_e$  profiles are then adjusted to match the measured values as the process is repeated.

### Probe Model Preliminary Results

Figures 2.14-2.16 show preliminary results of the above analysis for one set of experimental data. Figure 2.14 shows the Gaussian profiles of  $T_e(r)$  and  $n_e(r)$  that best reproduced the measured profiles of  $V_{d2}$  and  $I_3$ , along with the physical boundary of the exit plane and the thruster centerline. The width of  $n_e(r)$  corresponds to a standard deviation ( $\sigma$ ) of 3.0 mm, while the  $T_e(r)$  profile is much broader with  $\sigma=8.0$  mm. Figures 2.15 and 2.16 compare the measured and resulting predicted values of  $I_3$  and  $V_{d2}$ , respectively. These figures show good agreement in trends between the measured and predicted values, which is strong evidence that the quadruple probe measurements are being influenced by gradients in plasma parameters over the probe volume. The agreement is poorest far from the centerline, presumably because basic assumptions in the quadruple probe theory break down in this region. In particular, the

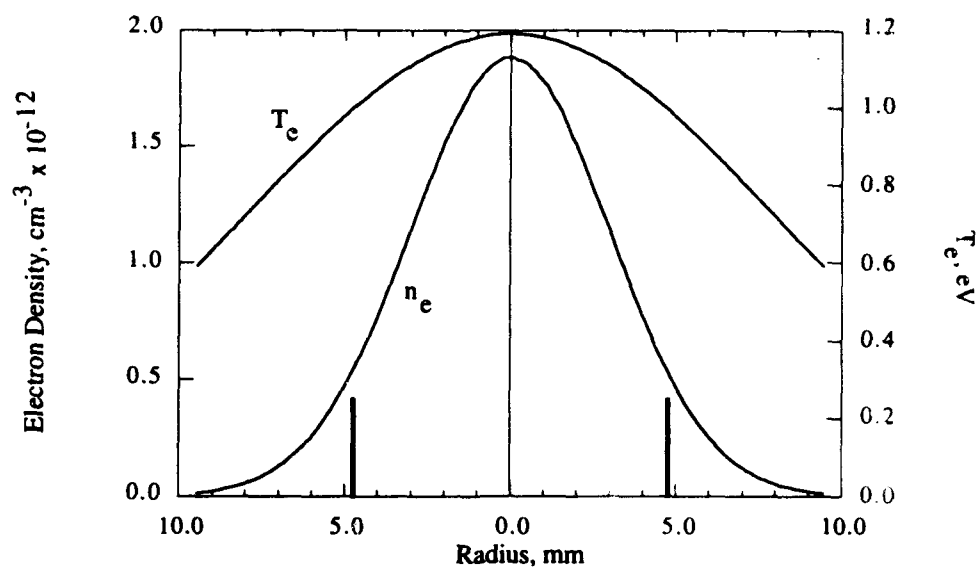


Fig. 2.14. Gaussian radial profiles of  $T_e$  and  $n_e$  at the thruster exit plane extracted from the measured values of  $I_3$  and  $V_{d2}$ .

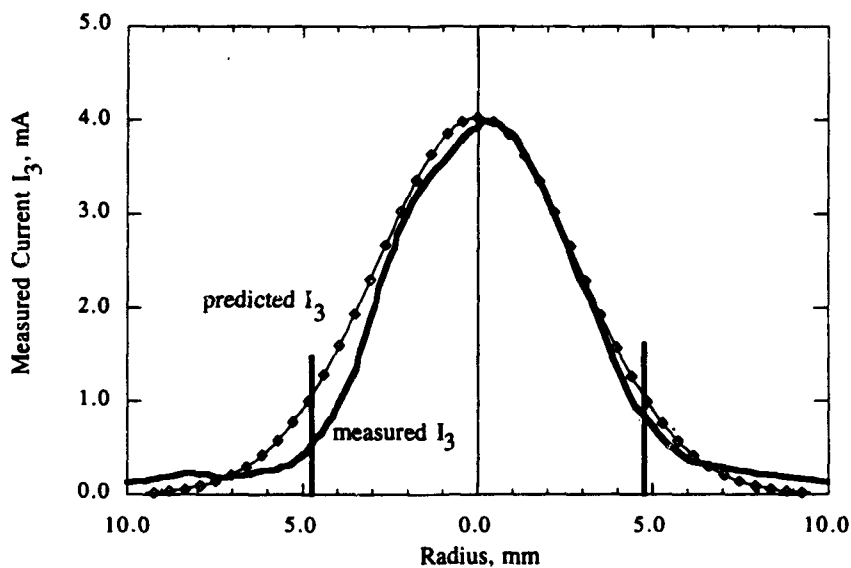


Fig. 2.15. Comparison of the measured  $I_3$  to the value predicted by the quadruple probe model for  $T_e(r)$  and  $n_e(r)$  with  $\sigma$  of 8.0 and 3.0, respectively.

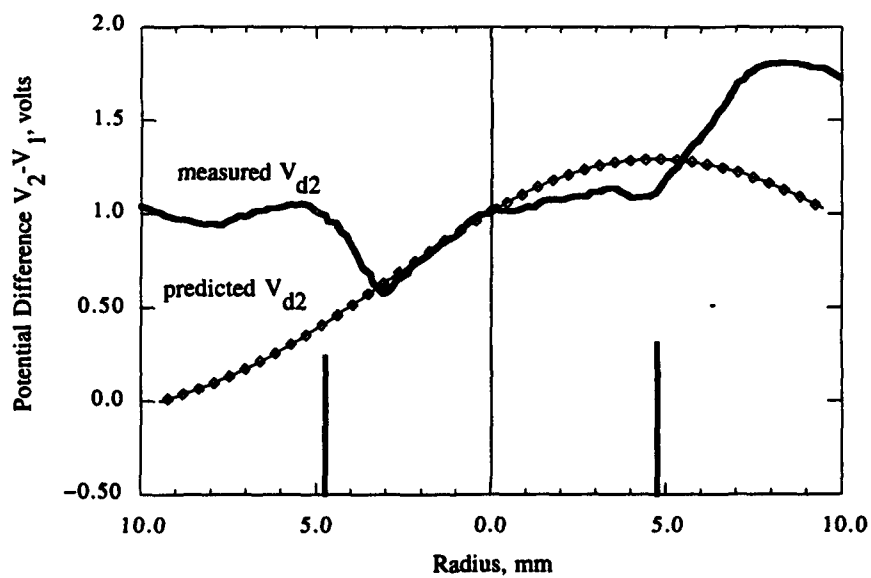


Fig. 2.16. Comparison of the measured  $V_{d2}$  to the value predicted by the quadruple probe model for  $T_e(r)$  and  $n_e(r)$  with  $\sigma$  of 8.0 and 3.0, respectively.

parallel probes are misaligned with the flow vector and the Debye sheaths around each electrode become thick and interact with each other far from the thruster centerline.

## Conclusions

Electrode sheath constraints prevent the construction of electrostatic probes that are small enough to avoid the problem of gradients of  $T_e$  and  $n_e$  over the probe size. In order to continue using this low-cost and robust measurement technique in small (large gradient) arcjet devices, it is necessary to understand how these gradients affect probe performance. In addition, it is necessary and desirable to be able to extract the profiles of  $T_e$  and  $n_e$  from the raw data (Fig. 2.8). To this end, the gradient model appears capable of replicating the asymmetric measured probe profiles inside the nozzle exit ( $0 < r < 5$  mm). Future versions of the model are being developed which will optimize the agreement between the measured and predicted values by varying the shape of the  $T_e$  and  $n_e$  profiles.



## 2.3 Electrostatic Probe Velocimetry

### Overview

In addition to the quantities  $n_e$  and  $T_e$ , quadruple probe measurements also yield the quantity  $u_i/c_m$  (= ion velocity / most probable thermal speed). Since  $c_m = (2kT_i/m_i)^{1/2}$ , knowledge of the heavy particle velocity  $u_i$  allows determination of the heavy particle temperature  $T_i$ . Recently, a low-cost method of measuring velocities in arcjet plumes has been developed and demonstrated by Spores, *et al.* on 1 kW hydrogen arcjets.<sup>8,18</sup> In this method, called Current Modulation Velocimetry (CMV), a short duration current spike is superimposed on the arcjet operating current. The effect of this current spike on the plasma is then monitored in a time-of-flight fashion as it is convected past two measurement positions in the thruster plume. This research will utilize a modified and improved version of the CMV technique, coupled with quadruple electrostatic probe measurements, to attempt to measure radial profiles of  $T_e$ ,  $n_e$ ,  $u_i$  and  $T_i$  in the near-field plume of a 1 kW arcjet.

### Review of the CMV Technique

In the work by Spores, *et al.*, a short duration current pulse was superimposed on the arcjet operating current.<sup>8,18</sup> Figure 2.17 shows the effect of one such current pulse on the arcjet current and voltage. Also shown in Fig. 2.17 is the periodic ripple associated with the arcjet current and voltage, which is a consequence of the switching nature of the arcjet power processing unit (PPU). The current and voltage ripple are 180° out of phase, which is a result of the negative impedance characteristic of the arcjet. The current pulse is initiated by momentarily closing a switch which introduces an RC circuit parallel to the arcjet. Upon switch closure, the arcjet voltage appears across the RC circuit, which charges over a few 1- $\mu$ s time constants. Since the current from the PPU is held constant over this time interval, the charging capacitor represents a short-lived current deficit in the arcjet. The arcjet current then rings sharply upward, significantly passing its previous maximum before it quickly damps to its normal PPU ripple.

It is believed that the positive ring of the current spike causes a momentary increase in electron recombination, which repopulates the uppermost energy levels. These electrons cascade downward, giving off radiation consistent with each electron transition. The propellant in the arc-heating region during the pulse is therefore "tagged." Velocity is inferred by measuring the time required for this tagged flow to traverse the distance between two observation points. In Refs. 8 & 18, this effect was monitored by measuring changes in H Balmer radiation at two different axial locations using photomultiplier tubes (PMT), Hydrogen Balmer-alpha notch filters

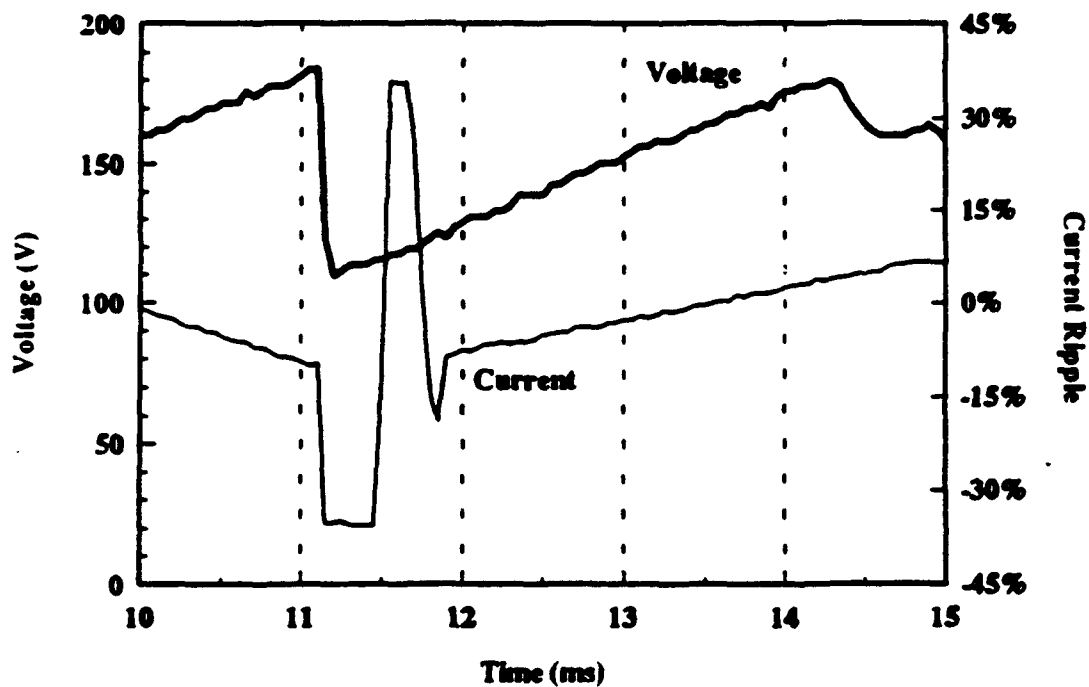


Fig. 2.17. Arcjet current and voltage traces showing the current pulse used in Refs. 8 & 18 and the periodic ripple associated with the arcjet PPU.  
(Taken from Spores, et al.<sup>18</sup>)

and the appropriate optics. The delay between the emission signals measured by each PMT is determined and related to velocity through the known detector control volume separation.

While optically monitoring the effect of the electron recombination usually proved useful in measuring plasma velocities, it was noted<sup>18</sup> that the positive ring of the current modulation did not always trigger the electron cascade phenomenon necessary to cause the requisite Balmer emission. In fact, it was found that for hydrogen arcjet operating voltages below a certain minimum voltage, the CMV technique described above did not work.

### **Modifications and Improvements in CMV for use at UIUC**

The optical (PMT) measurement technique used in Refs. 8 & 18, while non-intrusive, is a line-of-sight technique that precludes the direct measurement of spatially resolved velocities. The measured velocity is a radially integrated value over the PMT line-of-sight. This may explain the shape of the PMT signal profiles measured by Spores, *et al.* Both signals rise rather steeply initially ( $\sim 1 \mu\text{s}$ ) and fall off much more gradually ( $\sim 6 \mu\text{s}$ ). The sharp initial rise is possibly due to emission from the higher velocity centerline plasma, while both flow divergence and slower off centerline plasma may contribute to the gradually decreasing segment of the PMT signals. Ideally, a narrow width signal is desired for this type of measurement, and the wide shape of the signals from optical methods may introduce additional errors during calculation of the signal time delay.

As an improvement to the optical measurement methods described above and in Refs. 8 & 18, a time-of-flight electrostatic probe system will be utilized to measure the tagged plasma flow velocity. The electrostatic probe system affords several advantages over optical methods: 1) It is very low-cost and relatively robust, 2) Measurements can be spatially resolved, allowing measurements of velocity profiles, 3) Measured signal widths are likely to be narrow, making signal delays simpler to distinguish, 4) Momentary changes in basic plasma parameters ( $T_e$ ,  $n_e$ , etc.) can be monitored to indicate passage of the tagged flow, and 5) Successful velocity measurements are not contingent upon causing an optical event, a problem encountered by other researchers.<sup>8,18</sup>

### **Time-of-Flight Velocity Probe Preliminary Design**

Figure 2.18 is a schematic showing a preliminary concept for the time-of-flight sensing probe design. The probe, similar in construction to the quadrupole probe used for  $n_e$ ,  $T_e$  and  $u_i/c_m$  measurements, consists of two tungsten electrodes in line with the flow vector and electrically

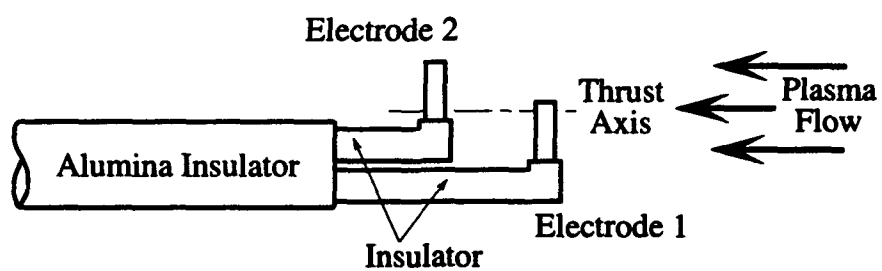


Fig. 2.18 Side view schematic of the time-of-flight electrostatic probe used for near-field plume velocity measurements.

insulated as shown. Although this probe is physically intrusive, appropriate length scales indicate that the probe electrodes (0.25 mm dia.) will be in the free molecular flow regime and are thus expected to have little effect on the flow. Previous experiments with the perpendicular electrode of the quadrupole probe have shown that an exposed electrode length of only a few millimeters provides sufficient collection area and signal strength. The two electrodes may be offset slightly (Fig. 2.18) to avoid an attenuation of the signal at electrode 2 due to the possibility of charge depletion<sup>19</sup> caused by current drawn at electrode 1, the upstream electrode. The axial probe separation is expected to be approximately 5 mm or less. However, the 10 MHz sampling speed of the existing data acquisition equipment may dictate a slightly larger distance in order to accurately resolve the time delay between the measured fluctuations at each electrode. To facilitate increasing the accuracy of the time delay measurement and decreasing the electrode axial separation, faster data acquisition equipment will be examined.

Monitoring natural fluctuations in the ion saturation current has been suggested<sup>9,20</sup> as a means of using time-of-flight electrostatic probes to measure velocities in perturbed plasma flows. This method is implemented, but instead will be used with artificially supplied current fluctuations. The two electrodes (Fig. 2.18) are biased sufficiently negative with respect to the plasma potential  $V_p$  that they each measure the local ion saturation current. From a particle flux standpoint, the saturation current is roughly proportional to the local charged particle density (and also collection area, particle velocity and particle charge). In previous work, Sankovic<sup>3</sup> showed that, for a 1 kW hydrazine arcjet, the electron density in the plume (~10 cm from nozzle exit) was a strong function of the thruster specific power. More specifically, it was demonstrated with steady state measurements that a 20% decrease in arc current caused nearly a 30% decrease in measured electron density. With quasineutrality, this corresponds to a similar change in ion saturation current. This is to be expected physically since changing the arc current changes the number of energetic electrons available for ionizing collisions. Therefore, superimposing a current pulse on the steady arcjet operating current is expected to cause a measurable fluctuation in the measured ion saturation current as the tagged flow passes each electrode.

Flow velocity will be calculated using the time delay between the ion saturation current signals measured at the two electrodes and the known electrode separation. The method of extracting the delay between the two signals is contingent on the shape of the signals. Two very sharply spiked signals would require little more than a visual inspection to determine the time lag. More realistically, the signals will have significant widths associated with them and the process will be more involved. In this case a numerical solution may be required to determine the time

delay, such as digitally performing a Fast Fourier Transform (FFT) autocorrelation routine on the two signals.

This method is attractive because the probe electronics can be rearranged in a very short time to measure the effect of the current pulse shape on other plasma parameters. The polarity of the probe bias can be switched so that the electrodes draw electron saturation current, which will produce a much stronger signal due to the larger mobility of the electrons. In addition, the effect of the pulse on  $T_e$  can be examined by measuring the floating potential  $V_f$  (relative to  $V_p$ ) of each electrode, since  $V_f$  varies approximately with  $T_e$ . Finally, a double probe configuration can be used, in which one electrode draws ion current while the other draws an equal amount of electron current. In this configuration a single channel can be monitored, which will show a fluctuation each time the tagged flow passes an electrode. Since changing configurations is simple, several can be attempted to check for agreement or to determine which is most feasible in terms of signal quality and/or data reduction.

### Introducing the Current Spike to the Arcjet Circuit

The arcjet electronic circuit is shown in Fig. 2.19. It consists of three components: a NASA LeRC arcjet power processing unit (PPU), a 1 kW arcjet, and a current modulation leg parallel to the thruster. The current modulation section of the circuit is connected through a MOSFET gate switch.<sup>18,21</sup> The MOSFET switch and its controller circuit are driven by a pulse generator, so that the switch closes for the duration of the pulse supplied by the pulse generator. Therefore, the duration of the current modulation can be varied by changing the width of the pulse supplied by pulse generator. The MOSFET controlled electrical switch shown in Fig. 2.19 may be used in conjunction with a variety of methods to create the current modulation to the arcjet.

A few variations on the current modulation result from changing the components in the dashed box (Fig. 2.19), as shown in Figs. 2.20a and 2.20b. Figure 2.20a shows the circuit used by Spores, et al.<sup>18</sup> Closing the MOSFET switch causes a momentary current loss to the arcjet, followed by the positive current "ringing" spike. It is this positive spike that causes the optical event measured in the above mentioned CMV papers. With electrostatic probes, however, the probes need only sense the changes in  $T_e$ ,  $n_e$  or electrode floating voltage  $V_f$  as the tagged flow passes the probes. Therefore, a simple resistive load may be sufficient for the purposes of the present research (Fig. 2.20b). A momentary closure of the MOSFET switch will cause a sudden and short-lived current deficit to the arcjet. As discussed above, this should cause significant density changes such that the effect of the current modulation will be measurable at the time-of-flight electrostatic probes.

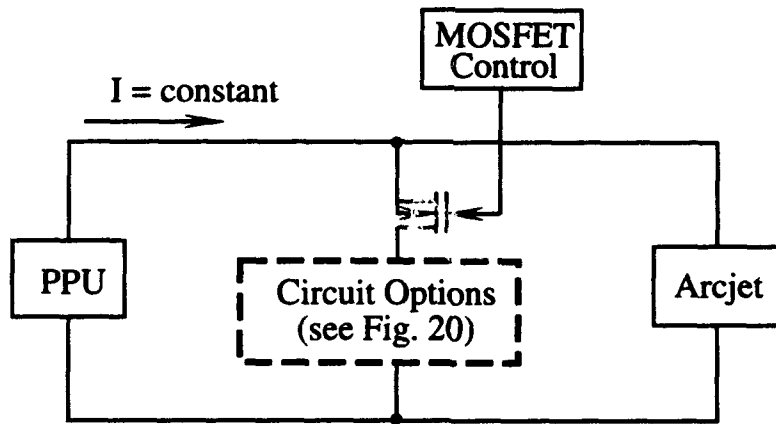


Fig. 2.19 Electrical circuit schematic for MOSFET gate controlled modifications of the arcjet current.

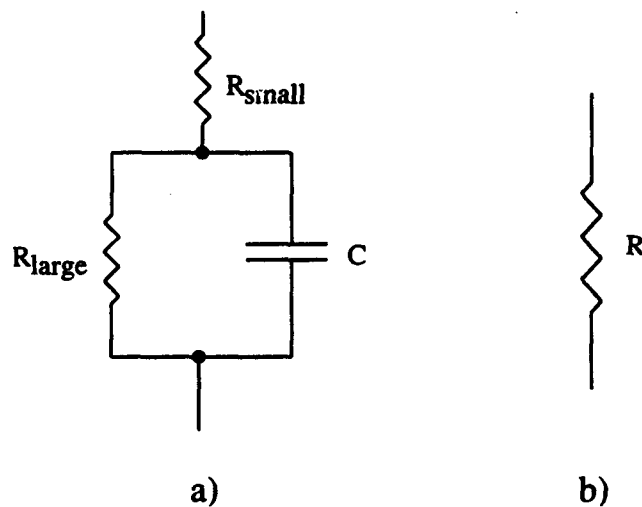


Fig. 2.20 Electrical circuit elements for causing the arcjet current pulse/deficit.

## References to Section 2†

- <sup>1</sup>Carney, L. M. and Keith, T. G., "Langmuir Probe Measurements of an Arcjet Exhaust," *Journal of Propulsion and Power*, Vol. 5, No. 3, 1989, pp. 287-294.
- <sup>2</sup>Carney, L. M. and Sankovic, J. M., "The Effects of Arcjet Operating Condition and Constrictor Geometry on the Plasma Plume," AIAA Paper 89-2723, July 1989.
- <sup>3</sup>Sankovic, J. M., "Investigation of the Arcjet Plume Near Field Using Electrostatic Probes," NASA TM-103638, Nov. 1990.
- <sup>4</sup>Sankovic, J. and Jankovsky, R., "An Experimental Investigation of the Effective Current Collecting Area of a Spherical Langmuir Probe in an Arcjet Thruster Exhaust," AIAA Paper 90-0073, Jan. 1990.
- <sup>5</sup>Langmuir, I. and Mott-Smith, H. M., "The Theory of Collectors in Gaseous Discharges," *Physical Review*, Vol. 28, 1926, pp. 727-763.
- <sup>6</sup>Chen, S.-L. and Sekiguchi, T., "Instantaneous Direct-Display System of Plasma Parameters by Means of Triple Probe," *Journal of Applied Physics*, Vol. 36, No. 8, 1965, pp. 2363-2375.
- <sup>7</sup>Tilley, D. L., Kelley, A. J. and Jahn, R. G., "The Application of the Triple Probe Method to MPD Thruster Plumes," AIAA Paper 90-2667, July 1990.
- <sup>8</sup>Pobst, J. A., Schilling, J. H., Erwin, D. A. and Spores, R. A., "Time Resolved Measurements of 1 kW Arcjet Plumes using Current Modulation Velocimetry and Triple Langmuir Probes," International Electric Propulsion Conference Paper 93-128, Sept. 1993.
- <sup>9</sup>Habiger, H. A., Auweter-Kurtz, M. and Kurtz, H., "Electrostatic Probes for the Investigation of Arc-Driven Electric Propulsion Devices," International Electric Propulsion Conference Paper 93-124, Sept. 1993.
- <sup>10</sup>Kanal, M., "Theory of Current Collection of Moving Cylindrical Probes," *Journal of Applied Physics*, Vol. 35, No. 6, 1964, pp. 1697-1703.
- <sup>11</sup>Bruce, C. and Talbot, L., "Cylindrical Electrostatic Probes at Angles of Incidence," *AIAA Journal*, Vol. 13, No. 9, 1975, pp. 1236-1238.
- <sup>12</sup>Johnson, B. H. and Murphree, D. L., "Plasma Velocity Determination by Electrostatic Probes," *AIAA Journal*, Vol. 7, No. 10, 1969, pp. 2028-2030.
- <sup>13</sup>Burton, R. L., DelMedico, S. G. and Andrews, J. C., "Application of a Quadruple Probe Technique to MPD Thruster Plume Measurements," *Journal of Propulsion and Power*, Vol. 9, No. 5, 1993, pp. 771-777.
- <sup>14</sup>Del Medico, S. G., "Plasma Flow Measurements by a Quadruple Probe in a Quasi-Steady MPD Plasma," M.S. Thesis, University of Illinois, 1992.
- <sup>15</sup>Nachtrieb, R. T., "Application of the Saha Equation to High Temperature (>6000 °K) Rocket Exhaust," Phillips Laboratory, PL-TR-92-3042, Edwards AFB, CA, Jan. 1993.



<sup>16</sup>Curran, F. M. and Haag, T. W., "Extended Life and Performance Test of a Low-Power Arcjet," *Journal of Spacecraft and Rockets*, Vol. 29, No. 4, 1992, pp. 444-452.

<sup>17</sup>Manzella, D. H., Curran, F. M., Myers, R. M. and Zube, D. M., "Preliminary Plume Characteristics of an Arcjet Thruster," AIAA Paper 90-2645, July 1990.

<sup>18</sup>Spores, R. A., Hargus, W. A., Pobst, J. A., Schilling, J. H., Lutfy, F. M. and Erwin, D. A., "Arcjet Diagnostics for Measuring Velocity, Density and Temperature," AIAA Paper 94-2464, June 1994.

<sup>19</sup>MacLatchy, C. S., "Charge Depletion Downstream of a Cylindrical Langmuir Probe Immersed in a Flowing, High-Pressure Plasma," *IEEE Transactions on Plasma Science*, Vol. 17, No. 1, pp. 29-33, Feb. 1989.

<sup>20</sup>Hoell Jr., J. M., Burlock, J. and Jarrett Jr, O., "Velocity and Thrust Measurements in a Quasi-Steady Magnetoplasma dynamic Thruster," *AIAA Journal*, Vol. 9, No. 10, pp. 1969-1974, Oct. 1971.

<sup>21</sup>Hamley, J., NASA LeRC Electrical Engineer, Private Communication, Aug. 1994.

<sup>†</sup>Reference numbers correspond to references in Section 2 of this document only.

## Section 3: Arcjet Energy Deposition in the Constrictor and Nozzle\*

### 3.1 Introduction

Improvements in the efficiency and performance of arcjet thrusters are achieved by understanding the fundamental energy input and loss mechanisms of the device. Since a typical low power arcjet nozzle is on the order of 1 cm in length, with particle speeds between 5-10 km/sec the charged particle residence time ( $\sim 10^{-6}$  sec) is much smaller than the recombination time. As a result, the flow is in chemical nonequilibrium, leading to frozen flow losses and a decrease in arcjet performance. Other factors that limit arcjet performance include thermal losses to the anode due to ohmic heating, current attachment, convection and radiation to the wall,<sup>1</sup> wall friction losses in the nozzle (due to large viscous and thermal boundary layer growth), nonuniform profile losses, electrode erosion and arcjet instabilities. The nozzle flow is very viscous ( $Re < 1000$ ) and highly nonequilibrium, with electron temperatures typically much greater than ion and neutral temperatures.

To achieve high specific impulse and thrust efficiency, the specific energy  $P/\dot{m}$  (input electrical power divided by propellant mass flow rate) must be increased. At high  $P/\dot{m}$  the anode overheats, so that improvement of arcjet performance for all power levels relies on understanding the interaction between the plasma and the anode wall.<sup>1</sup>

In both the constrictor and nozzle regions, energy transport from the plasma to the walls is a strong function of the electron number density and temperature distributions. Nonequilibrium processes determine the spatial variation in current attachment and anode heating. Such processes dominate in the thick boundary layer, so that measurements of local  $n_e$  and  $T_e$  inside the boundary layer will be helpful in understanding the current attachment and energy deposition between the plasma and the anode. The distributions of current density, electric field and voltage are also poorly understood, and are strongly coupled to the  $n_e$  and  $T_e$  distributions near the constrictor and anode walls.

Due to the thick viscous and thermal boundary layers present in the nozzle, the plasma core flow and boundary layer processes are coupled. The volumetric ohmic heating,  $j^2/\sigma$ , determines where the energy is deposited, which in turn determines the electrical conductivity  $\sigma(n_e, T_e)$ . This electrical conductivity distribution then prescribes the voltage and current distributions, which affect the arc attachment and the thermal losses to the anode. Also, viscous effects in the boundary layer are coupled with the plasma core flow.

---

\*Ph.D. Candidate, Nicholas T. Tiliakos, leads our research group in developing internal diagnostics for the arcjet.

### 3.2 Research Approach

The main objective of this research is to understand the fundamental physical processes governing energy deposition in the constrictor and nozzle regions of a low power, 2 kW hydrazine arcjet. This involves: (1) using Langmuir probes for internal arcjet diagnostics, (2) determining the ohmic heating distribution in the arcjet and what conditions govern its distribution, (3) understanding the physical mechanisms concerning current attachment and therefore anode heating, and (4) validating the UIUC arcjet model (Section 1).

To accomplish these objectives local electron number density and electron temperature measurements using flush-mounted Langmuir probes will be made at several axial and azimuthal locations in the nozzle and constrictor regions. Current density measurements will also be made, while using the Langmuir probes as conducting pins. In addition, spectroscopic measurements will be performed in the nozzle plasma core flow (see Section 3.5). Flush-mounted Langmuir probes will not only obtain data in the constrictor, but also near the constrictor exit, 1.5 mm downstream. Such data ( $n_e$ ,  $T_e$ ,  $j$ ) in close proximity to the constrictor is very important, since it has been found that the arcjet operation is stable when the arc attaches in the supersonic region just downstream of the constrictor exit.

### 3.3 Previous Research

The first experimental investigations of the nozzle region of a low power arcjet were conducted at the NASA-Lewis Research Center. Zube *et. al*<sup>2</sup> were the first to perform emission spectroscopy of the plasma flow inside the nozzle of a 1 kW hydrazine arcjet. Several 0.25 mm holes were drilled into the diverging section of the nozzle, providing optical access to the internal flow. Measurements included atomic electron excitation, vibrational and rotational temperatures for the expanding plasma using the relative line intensity techniques. However, no data were obtained inside the constrictor region and the closest data point was 2.4 mm downstream of the constrictor.

To date, emission spectroscopy has been the main diagnostic used for internal probing of the arcjet. Measurements of plasma conditions inside the constrictor have been performed on medium power arcjets (5-20 kW).<sup>3,4</sup> In the work of Zube *et.al*<sup>3</sup> the constrictor had a 2 mm radial hole covered by a quartz window for optical access. Spectroscopic measurements included radial profiles of H<sub>2</sub> excitation temperature, electron density and atomic hydrogen density in the

constrictor. However, due to problems with line width determination near the walls only the data from the inner 60-70 % of the constrictor diameter gave reliable results.<sup>3</sup> A problem with this type of configuration is heat transfer and temperature restrictions on the window, which make it unrealistic to relate such results to flight-type thrusters.<sup>2</sup>

Curran *et.al*<sup>5</sup> have studied arc energy deposition in the nozzle, the nature of arc attachment, and its effects on performance characteristics of the device. They used a 1-2 kW arcjet that incorporated a segmented anode nozzle with 5 axial conducting segments isolated from each other by boron nitride spacers. The current to each segment and the potential difference between each segment and the cathode were measured. The current was found to attach diffusely to the nozzle wall, with more than 50% of the input power added in the diverging section of the nozzle. The current distribution was found to be dependent on the mass flow rate. We will perform current density measurements similar to Curran, using conducting pins (~.015" diameter) embedded in a monolithic anode, thus minimizing disruptions to the anode's heat flow.

Very little experimental work has focused on investigating azimuthal symmetry in the current density distribution inside a low power arcjet. Harris *et.al*<sup>6</sup> have studied anode arc motion in a water-cooled radially segmented 30 kW arcjet. It was found that the azimuthal current distribution in an arcjet nozzle is asymmetric. With our conducting pin configuration, we will be able to measure azimuthal current density, thus determining whether the current distribution is symmetric in the 2 kW arcjet.

### 3.4 Langmuir Probe Theory

Langmuir probes have been a powerful means of plasma diagnostics since the early 1920's, when the method was first implemented by Irving Langmuir and his co-workers.<sup>7</sup> This type of probe consists of a small metallic electrode (wire) inserted into a plasma. The probe is connected to a variable power supply, allowing the probe to be biased at various positive/negative voltages with respect to the plasma. The current collected by the wire is then measured as a function of the biasing probe voltage, generating a probe characteristic (Fig. 3.1), and providing information on the plasma conditions.

The electron number density and electron temperature can be obtained from a probe characteristic, assuming collisionless, thin sheath, Langmuir probe theory. A thin sheath means that the probe's sheath thickness is much smaller than the probe radius. The probe's sheath thickness is on the order of several Debye lengths,  $\lambda_D$ . The Debye length is the distance over

which the perturbing effects of a charge will tend to penetrate into a plasma. For  $n_e = 2 \times 10^{20} \text{ m}^{-3}$ , and  $T_e = 1.9 \text{ eV}$  ( $\sim 22,000 \text{ }^\circ\text{K}$ ),  $\lambda_D = .71 \text{ microns}$ , which, compared to a  $.015''$  (381 microns) probe diameter, means that this is a thin probe sheath.

Region 'A', (Fig. 3.1), is called the electron saturation region, where the probe voltage,  $V_p$ , is greater than the plasma space potential,  $V_s$ , thereby attracting electrons to the probe and repelling ions. A layer of charge builds up on the probe forming an electron sheath. In the sheath layer the plasma is no longer quasi-neutral, the number density of electrons and ions are not equal so that large electric fields exist. Outside the sheath the electric field is small so that the plasma is essentially undisturbed and quasi-neutral. Region 'A' provides the magnitude of the electron saturation current.<sup>8</sup>

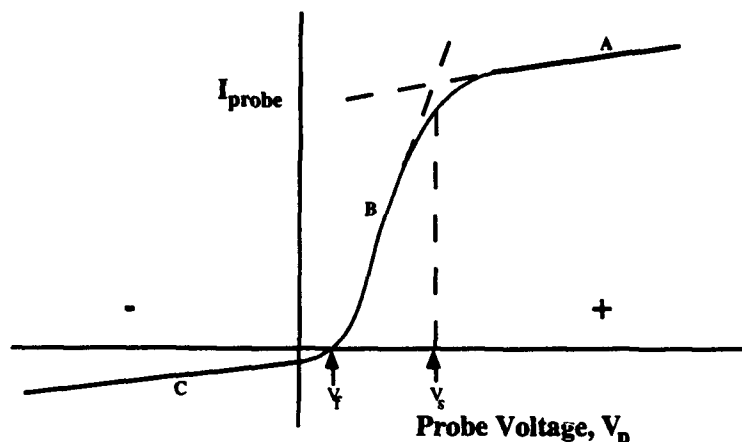


Fig. 3.1 Schematic of a typical probe characteristic, showing the various regions of interest that provide information on the plasma conditions. [Reference 8]

When the probe voltage equals the plasma space potential,  $V_s$ , there is no net voltage gradient around the probe, and no sheath exists that repels the electrons. As a result the charged particles migrate to the probe because of their random thermal velocities. In region 'B', the Transition Region, the probe voltage is made negative relative to the plasma space potential so that low energy electrons are repelled and ions are accelerated to the probe. If the electron distribution were Maxwellian, then the shape of the Transition Region on a  $\log(I_{\text{probe}} - I_{\text{ion.sat.}})$  versus  $V_p$  plot would be linear, with the slope providing the electron temperature, as given in Eq. (3.1).<sup>9</sup> Once the electron temperature is known, the electron number density is found from the magnitude of either the ion or electron saturation current, as given in Eq. (3.2):<sup>9</sup>

$$T_e = \frac{e(I - I_{\text{ion.sat.}})}{(dI/dV_o)} \quad (3.1)$$

$$n_e = \frac{I_{ion.sat.}}{(0.61)eA_p(T_e/m_i)^{1/2}} \quad (3.2)$$

where  $A_p$  is the probe area,  $I_{ion.sat.}$  is the ion saturation current,  $m_i$  is the ion mass and  $dI/dV_0$  is the slope of the probe characteristic of the  $\log(I_{probe} - I_{ion.sat.})$  versus  $V_p$  plot (in Region 'B').

When the probe potential equals the floating potential,  $V_f$ , the flux of electrons equals the flux of ions to the probe so that the net current is zero. This is equivalent to inserting a wire, without applying a biasing voltage, into a plasma.

In region 'C', the ion saturation region, almost all electrons are repelled, resulting in an ion sheath. The ion saturation current is much less than the electron saturation current because the electron mass is  $\sim 1000$  times smaller than the ion mass and  $T_e \gg T_i$ .

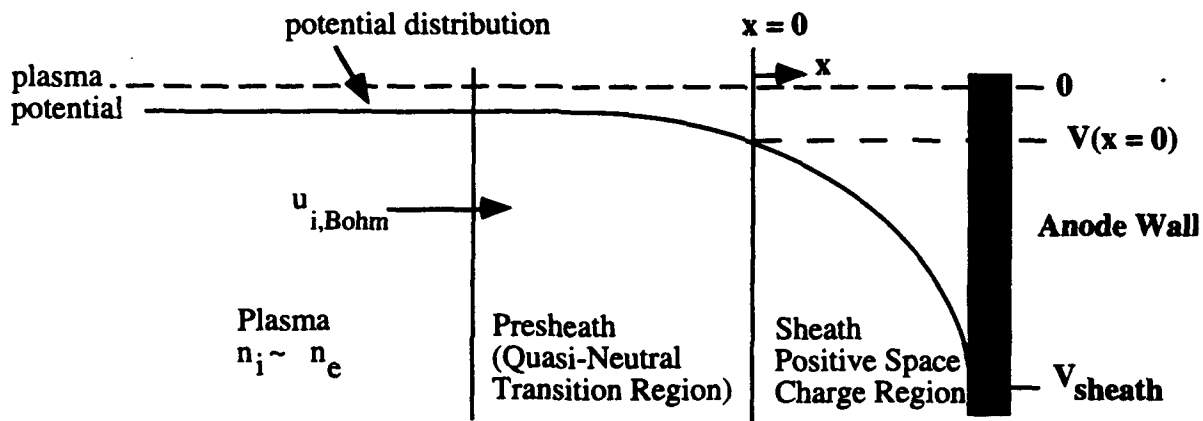


Fig. 3.2 Schematic of the anode-plasma interface depicting sheath formation and the presheath transition region. This sheath formation is for a grounded anode, surrounded by an electropositive plasma.

Figure 3.2 shows the sheath formation at the anode. A sheath forms at the anode-plasma interface due to a potential drop between the anode and the plasma. Near an electrode there are not enough collisions to randomize the electron and ion flux, and a sheath forms to shield the bulk plasma from this region of non-neutrality. There is also a transition region between the sheath and the plasma known as the presheath. In order to satisfy Poisson's equation in the sheath, the ions must enter the presheath with the Bohm velocity,  $u_{i,Bohm}$ . The potential drop at the anode/plasma interface can be as much as -15 Volts.

Langmuir probes are easy to implement since they are relatively simple devices, but interpreting the probe characteristic can be difficult, especially if there are ionization and collisional reactions occurring inside the sheath. If the probe sheath is collisional (i.e. if the charged particle mean free path  $\ll \lambda_D$ ) then the Langmuir probe theory requires modification, since collisions reduce the current to the probe because particles diffuse up to the probe instead of arriving there by free flight.<sup>9</sup>

Figure 3.3 shows a schematic of plasma flow over a flush-mounted Langmuir probe inside the arcjet nozzle. There are three regions of interest: (1) the nozzle viscous boundary layer, (2) the anode sheath, and (3) the probe sheath. Initially, when the probe is not biased, the anode and the probe sheaths coincide. As the probe is biased positive or negative a separate sheath forms, surrounding the probe. The Langmuir probe measurements of  $n_e$  and  $T_e$  are thus local measurements, i.e. inside the anode boundary layer.

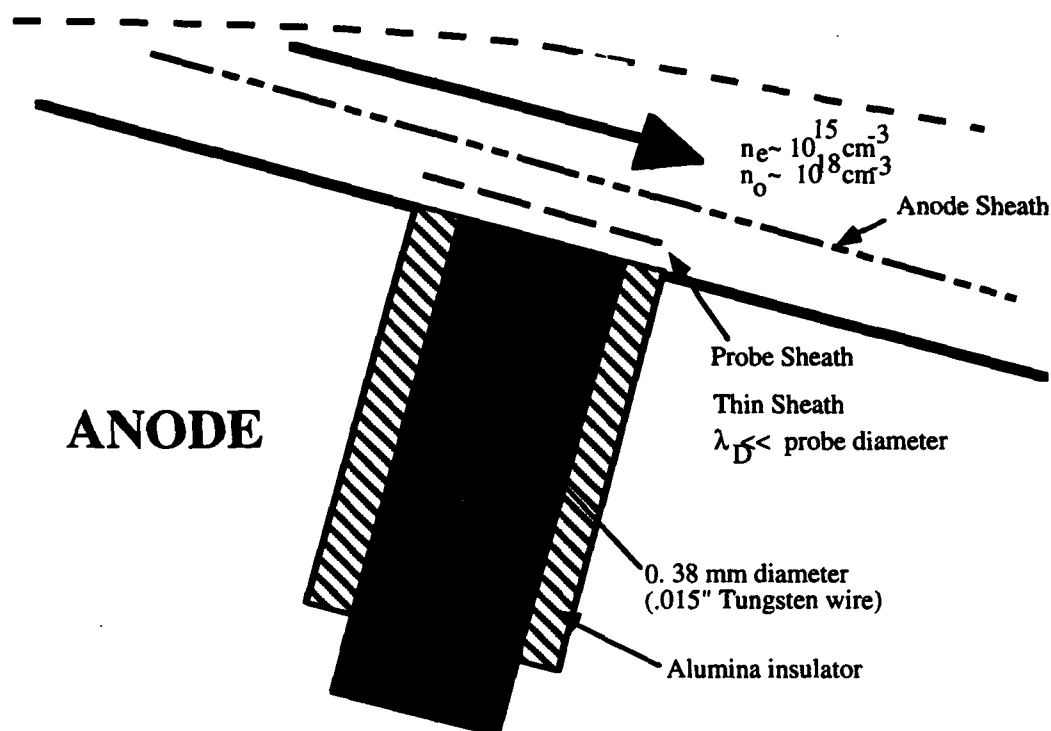


Fig. 3.3 This figure shows the plasma flow over the flush-mounted Langmuir probe inside the boundary layer. A separate anode and probe sheath form.

A variation on the Langmuir probe is the double Langmuir probe, which consists of two probes connected to a biasing voltage supply with typical voltage sweep rates on the order of 100  $\mu\text{sec}$ .<sup>10</sup> Analysis of the characteristic, similar to the single probe, provides measurements of  $n_e$  and  $T_e$ .<sup>9</sup> The benefit of a double Langmuir probe (or a "floating" double probe) is that it minimizes

electron current collection. Consequently, the total current to the probes can never be greater than the ion saturation current, minimizing the disturbance on the plasma discharge, and preventing overheating of the probe.

### 3.5 Experimental Approach

A monolithic anode 2 kW hydrazine arcjet thruster has been fabricated at the University of Illinois (Fig. 3.4). The thruster anode is machined from a tungsten alloy, HD 18 (95% W, 3.5% Ni, 1.5% Fe) which is easier to machine than thoriated tungsten, the conventional arcjet anode material. The monolithic anode eliminates the front seal, simplifying heat transfer analysis.

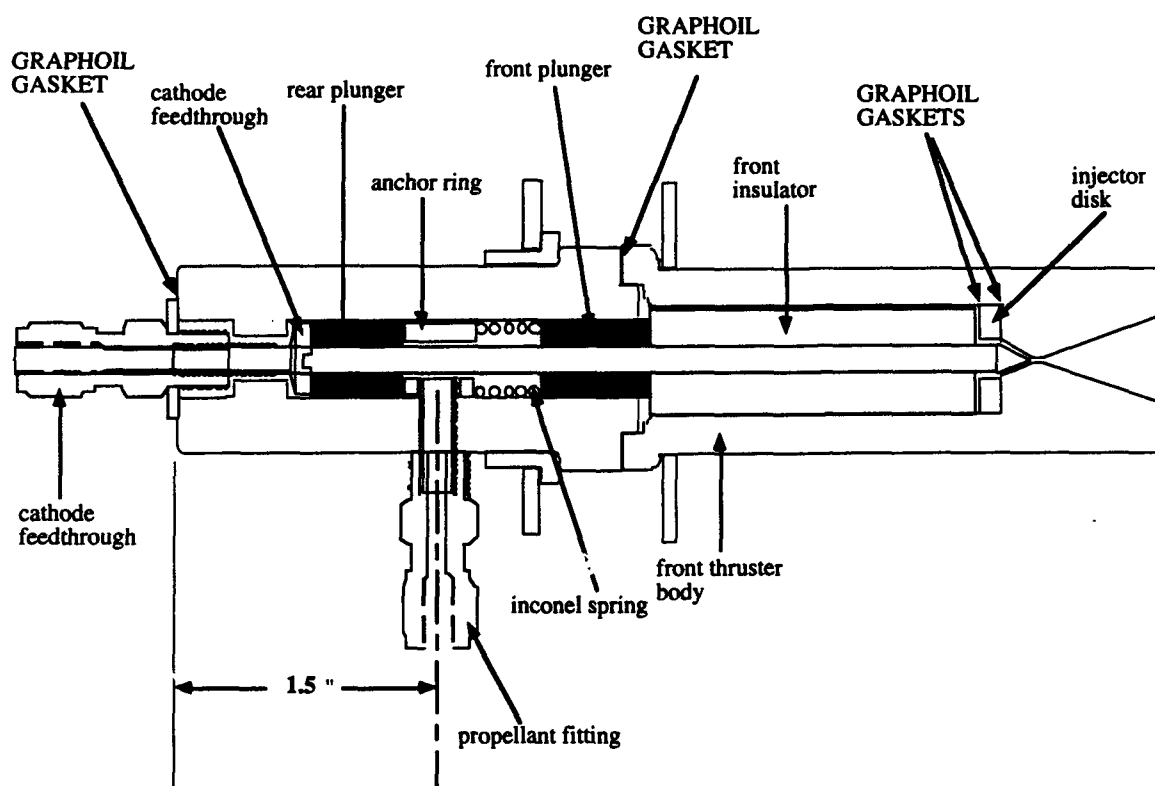


Fig. 3.4 The new UIUC 2 kW hydrazine arcjet thruster.

To obtain electron number density and electron temperature measurements in the arcjet boundary layer, flush-mounted single and double Langmuir probes will be installed in the constrictor and nozzle wall. The constrictor diameter has been increased to 1.0 mm, up from 0.64 mm for the 1 kW thruster, and the constrictor length is now 1.5 mm, up from .25 mm. The larger scale thruster can incorporate an array of Langmuir probes, as shown in Fig. 3.5. The probes are



mounted to the nozzle through vacuum sealed male connectors. The 2 kW thruster is seated on a mounting pod inside a 1.5 m<sup>3</sup> vacuum tank, with a background pressure of ~ 100 mTorr for flow rates of 50 mg/sec.

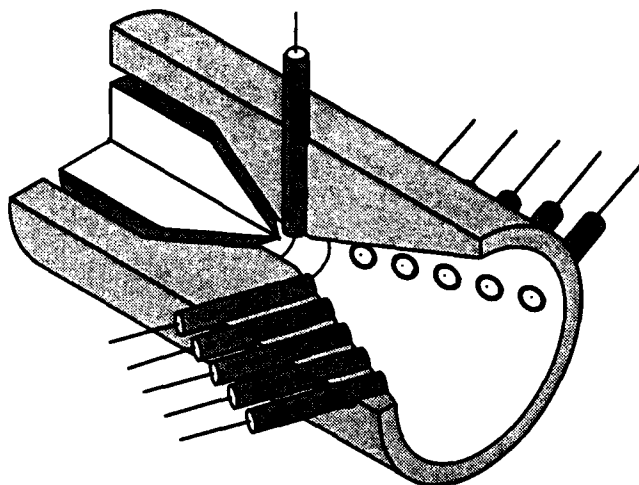


Fig. 3.5 Cross-sectional schematic of a typical arcjet configuration, with an array of Langmuir probes inside the constrictor and nozzle walls.

Once thruster operating characteristics have been determined, the anode body will undergo additional machining to accommodate the single and double flush-mounted Langmuir probes. Initial experimental tests will implement the single probes. These probes are made of tungsten wire, surrounded by an alumina insulator, and inserted in a stainless steel tube. In the constrictor there is one probe with diameter .007 " (.18 mm), while in the nozzle wall there can be at most six probes, two at the same axial location, but different azimuthal location (separated by 90°), with diameter .015 " (0.38 mm). The probes will be biased with a function generator sweeping between  $\pm 12$  volts. A power op-amp will be used to isolate the probe from the function generator in order to avoid drawing excessive current from the function generator.

The next phase of the experiment will involve using double Langmuir probes and perhaps implementing more probes at different locations inside the nozzle. To obtain the distribution of ohmic heating in the nozzle region the current density will be measured along the nozzle wall. This is done by measuring the current to each of the Langmuir probes, which for this case are now just conducting pins connected directly to the anode. Knowing the cross-sectional area of each pin the current density distribution along the nozzle is obtained. The current density measurements, coupled with calculations of the electrical conductivity distribution (based on  $n_e$ ,  $T_e$  measurements)

provide an estimate of the ohmic heating,  $j^2/\sigma(n_e, T_e)$ , at various axial locations inside the boundary layer. Calculations of the electrical conductivity will also lead to the voltage distribution along the nozzle wall.

Spectroscopic measurements may eventually be required to obtain  $n_e$  and  $T_e$  profiles in the plasma core flow in the nozzle. These measurements would be made through a series of open holes in the nozzle wall. Emission spectroscopy will require use of an Optical Multichannel Analyzer (OMA). Other diagnostics would include static pressure measurements along the constrictor and nozzle walls.

The final phase of the experiment will require modifying the UIUC arcjet model to include applied magnetic field effects and observing how the field affects  $n_e$ ,  $T_e$  and  $j$  distributions. Based on the numerical results a magnetic bobbin can be designed and used as a diagnostic tool.

Last year an investigation of a pulsed magnetic field on the operation of a NASA 1 kW arcjet was conducted in the 1.5 m<sup>3</sup> tank at the UIUC Electric Propulsion Laboratory.<sup>11</sup> We found that during the duration of the pulse the arcjet voltage increased by as much as 6 volts. Similarly, for a given magnetic field strength, as the propellant flow rate was decreased the change in arcjet operating voltage due to the magnetic field increased. This preliminary work suggested that a magnetic field could be used to control the current attachment location, i.e. the electron drift motion, and therefore the heating inside the arcjet.

Some possible effects of an applied magnetic field include decreasing thermal losses to the anode wall, since the electron thermal conductivity scales as  $\Omega_e/(1 + \Omega_e^2)$  where  $\Omega_e$  is the electron Hall parameter (proportional to the magnetic field strength). Also, propellant swirl would be increased due to the  $j_r B_z$  and  $j_z B_r$  Lorentz forces; this would enhance mixing and arc stability. Similarly, particle residence time would increase, allowing more time for recombination to occur.<sup>11</sup>

A steady state applied field, using a pulsed magnet in series with the arcjet, can be used to modify the current distribution in a predictable way, and can therefore assist in further validating the UIUC arcjet model (Section 1). Magnetic field strengths of several 100 Gauss can be achieved on the nozzle centerline. The UIUC code will be modified to include the effects of an externally applied magnetic field. This will involve incorporating analytic expressions for the externally applied magnetic field, which has components  $B_r$  and  $B_z$ .

This investigation will involve use of the UIUC arcjet model comparisons with the experimental results. The numerical model will also assist in directing the experimental work.

Initially, the model will be used to predict electron number density, electron temperature and current density distributions in the nozzle region for various propellant flow rates and propellant mixtures. The mole fraction of  $N_2$ ,  $x$ , is also an input parameter, since the propellant can be described as  $xN_2 + H_2$ . If  $x = 0$  then the propellant is  $H_2$ , while if  $x = 0.5$  the propellant is simulated hydrazine. This leads to a flexible model that can predict arcjet performance for ammonia, hydrogen and simulated hydrazine propellants. This variation in propellant type can be implemented in the laboratory as well. The model predictions for  $n_e$ ,  $T_e$ ,  $j$  and  $\sigma$  distributions will then be compared with the experimental data in the constrictor and nozzle regions.

### 3.5.1 Experimental Procedure

Figure 3.6 shows a schematic of the probe experiment. The probe supply consists of a function generator that sweeps the Langmuir probe between  $\pm 15$  V. A power op-amp will be used as an isolation stage between the probe and the function generator. The tests will be run during the 20 minute arcjet warm-up period to minimize probe thermal loading.

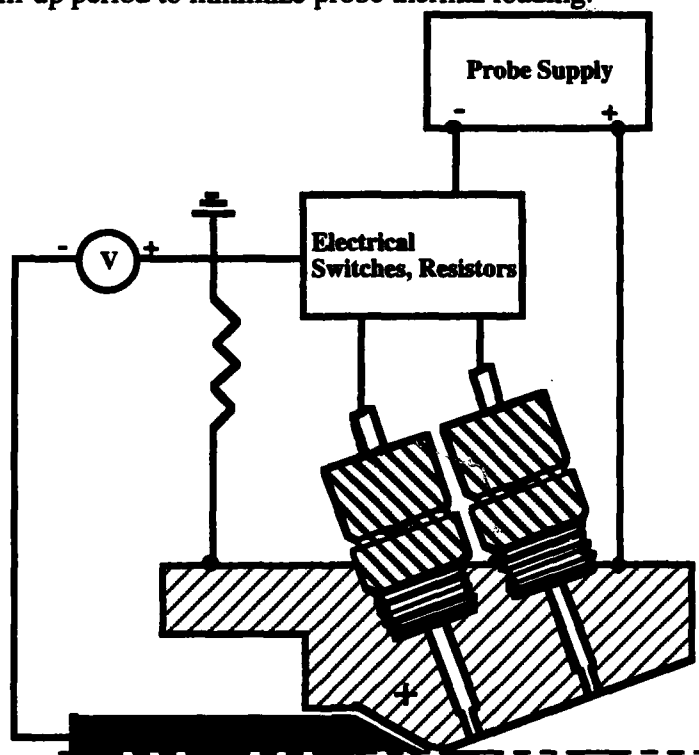


Fig. 3.6 Schematic of Langmuir probe/conducting pin experiment.

The probe current is obtained by measuring the voltage drop across a known resistance, while the probe voltage is measured by a voltage probe connected to a 10 MHz SOLTEC oscilloscope. The SOLTEC oscilloscope will be set to acquire data for a period at least as long as it takes the function generator to sweep  $\pm 15$  V. The data it will obtain is probe voltage vs time and

$\Delta V_R$  vs  $i$  where  $\Delta V_R$  is the voltage drop across a known resistance,  $\sim$  probe current. The two channels for probe voltage and  $\Delta V_R$  vs time are cross plotted to obtain the probe characteristic.

### 3.5.2 Some Important Probe Considerations

Some of the consequences of physical probing of the hostile arcjet environment include probe contamination, probe surface reactions and probe heating.

#### Probe Contamination/Surface Considerations

(1) Thermionic emission of electrons from the probe's surface can lead to a perturbation to the probe's electric field. As a result these emission currents could greatly perturb the potential distribution in the neighborhood of the probe, thereby invalidating any probe theories used that do not take emission currents into account. In order for thermionic emission effects to be negligible the probe temperature should never exceed 1200 °C (1473 °K).<sup>12</sup> This may be particularly important for probes near the constrictor region where the temperatures are expected to be highest.

(2) If the probe is at a different temperature than the plasma this could lead to a perturbation to the concentration and temperature of the carriers and neutrals.<sup>13</sup> As a result of these temperature gradients, heat and mass flow occurs. This should not be a problem for our design since the probe is insulated in alumina, which conducts heat well, and also because the probe is small relative to the nozzle wall in which it is embedded; as a result, the probe will approximately equal the anode wall temperature. The nozzle wall, in turn, is in good thermal contact with the plasma.

Since the probe tip receives the greatest energy flux it is usually made out of a refractory metal such as platinum, molybdenum or tungsten.<sup>9</sup> In our investigation the probe will be made of tungsten.

Problems with the probe's surface can lead to plasma perturbations resulting in errors in the measurement of current density or probe potential. Some of these problems include:

(1) The probe surface may be involved in direct chemical reaction or catalysis in chemically active plasmas, resulting in perturbations in both plasma composition and temperature. This is not a problem for us since the plasma is not chemically reacting with the probe surface.

(2) Sputtering of the probe's surface material can lead to uncertainties in the probe's effective collecting area, carrier reflection and emission from the surface, leading to errors in the current density measurement. If the sputtered material is in electrical contact with the probe there will be an under-estimation of the effective collecting area of the probe. Similarly, if the insulating material sputters onto the probe's surface there could be an over-estimation of the effective collecting area.<sup>13</sup> One way to avoid problems with changing the effective area of the probe is to center the probe tip in the insulator so that the point of contact with the insulator is well away from the plasma.<sup>9</sup>

### Probe Heating

In considering sizing of the probe and the experimental procedure of obtaining the probe characteristic, we must account for the maximum heat load that the probe can tolerate. This is particularly important if the electron saturation portion of the characteristic is obtained.

To avoid over-heating the probe, especially when collecting electrons, the probe voltage will be pulsed. The pulse begins at  $t = 0$ , resulting in an increase in probe temperature,  $\Delta T_w$ , given by subscript 'w', which refers to tungsten probe properties. A simple calculation of the temperature rise profile of the probe is given by the following equation:<sup>14</sup>

$$\Delta T_w = \frac{2qt^5}{(\pi\rho_w c_w \kappa_w)} \quad (3.3)$$

where  $q$  is the heat flux to the probe assumed to be constant and equal to:

$$q = \frac{V_{e,sat} I_{e,sat}}{A_{probe}} = \frac{V_p I_{e,sat}}{A_{probe}} \quad [W/m^2] \quad (3.4)$$

It is assumed that the electron saturation voltage is approximately equal to the plasma potential, which is very small ( $\sim O(1)$  mV). The calculation is made for conditions just downstream of the constrictor and for the electron-saturation region of the probe characteristic, which are worst case conditions. The results are shown in a plot of  $\Delta T_{probe}$  versus time for three different plasma potentials, Fig. 3.7. The results suggest that we should pulse the probe on and off when near the electron saturation region, because the probe may heat up to as much as  $1250^\circ K + \Delta T_{probe}$  or about  $1500^\circ K$ . The probe must never exceed about  $1473^\circ K$  ( $1200^\circ C$ ) to ensure that thermionic emission from the probe is negligible.

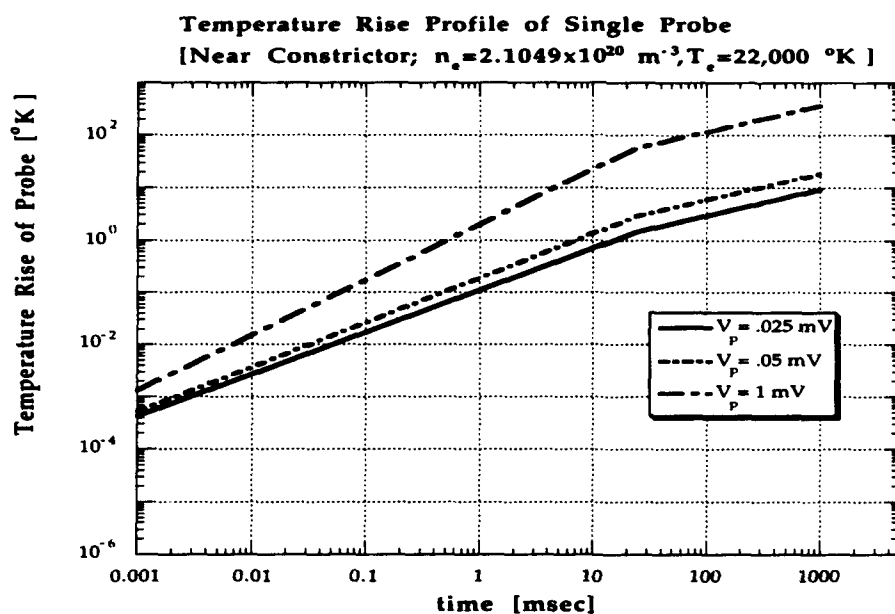


Fig. 3.7 Temperature rise profile of a single Langmuir probe for various assumed plasma potential values. To prevent excessive probe heating the probe biasing voltage should be swept at a frequency corresponding to  $\Delta T_w = 20^\circ$ .

### References to Section 3

- (1). Hoskins, W.A., Kull, A.E., and Nesser, W.M., "Measurement of Energy Deposition Modes in an Intermediate Power Hydrogen Arcjet," IEPC-93-216 AIAA/AIDAA/DGLR/JSASS, 23<sup>rd</sup> International Electric Propulsion Conference, Sept. 1993, Seattle, WA.
- (2). Zube, D.M., and Myers, R.M., "Nonequilibrium in a Low Power Arcjet Nozzle," AIAA-91-2113, AIAA/SAE/ASME/ASEE, 27<sup>th</sup> Joint Propulsion Conference, June 1991, Sacramento, CA.
- (3). Zube, D.M., and Auweter-Kurtz, M., "Spectroscopic Arcjet Diagnostic Under Thermal Equilibrium and Nonequilibrium Conditions," AIAA-93-1792, AIAA/SAE /ASME/ASEE, 29<sup>th</sup> Joint Propulsion Conference, June 1993, Monterey, CA.
- (4). Glocker, B., and Auweter-Kurtz, M., "Numerical and Experimental Constrictor Flow Analysis of a 10 kW Thermal Arcjet," AIAA-92-3835, AIAA/SAE/ ASME/ASEE, 28<sup>th</sup> Joint Propulsion Conference, July 1992, Nashville, TN.
- (5). Curran, F.M., Manzella, D.H., and Pencil, E.J., "Performance Characterization of a Segmented Anode Arcjet Thruster," AIAA-90-2582, AIAA/DGLR/JSASS, 21<sup>st</sup> International Electric Propulsion Conference, July. 1990, Orlando, FA.
- (6). Harris, W.J., O'Hair, E.A., Hatfield, L.L., Kristiansen, M., and Mankins, J.S., "Anode Arc Motion in High Power Arcjets," AIAA-92-3838, AIAA/SAE/ASME/ASEE, 28<sup>th</sup> Joint Propulsion Conference and Exhibit, July 1992, Nashville, TN.
- (7). Langmuir, I., and Mott-Smith, H.M., Gen. Elec. Rev. Vol. 26, 1923, pp. 731; Vol. 27, 1924, pp. 449, 583, 616, 726, 810; Phys. Rev., Vol. 28, 1926, pp. 727.
- (8). Huddleston, R.H., Plasma Diagnostic Techniques, Academic Press New York, 1965 (Chapter 4 by F.F. Chen).
- (9). Hutchinson, I.H., Principles of Plasma Diagnostics, Cambridge University Press, 1987.
- (10). Dunn, M.G., "Electron-Density and Electron Temperature Measurements in Boundary Layers," *AIAA Journal*, Vol. 9, No. 8, August 1971, pp. 1561-1567.
- (11). Tiliakos, N.T., and Burton, R.L., "Effect of a Pulsed Magnetic Field on Arcjet Operation," IEPC-93-186, 23<sup>rd</sup> International Electric Propulsion Conference, Sept. 1993, Seattle, WA.
- (12). Soulas, G.C., and Myers, R.M., "Mechanisms of Anode Power Deposition in a Low Pressure Free Burning Arc," IEPC-93-194, 23<sup>rd</sup> International Electric Propulsion Conference, Sept. 1993, Seattle, WA.
- (13). Swift, J.D., and Schwar, M.J.R., Electrical Probes for Plasma Diagnostics, New York American Elsevier Publishing Company, 1969, pp. 220-245.
- (14). Tidman, D.A., and Goldstein, S.A., "Thermal Transport to Hypervelocity Gun Tubes by High Pressure Partially Ionized Gas Flows," GT-Devices Technical Note GTD 85-4, May 1985, pp. 22-23.

## Appendix A Nitrogen Ion Density in Non-Equilibrium Hydrazine Arcjets

It has been observed experimentally by Keefer et al.<sup>1</sup> and Hargus et al.<sup>2</sup> that unusually low nitrogen densities are found downstream of the constrictor in ammonia and hydrazine arcjets. It is suggested that this is a result of charge exchange collisions in the expanding nitrogen-hydrogen propellant.

Number density ratios for nitrogen and hydrogen atomic and ionic species are shown in Fig. A.1. Calculations are for a weakly ionized hydrazine plasma in thermal ( $T_e = T_g$ ) and chemical equilibrium at  $p = 1$  atm. For gas temperatures below  $T_g = 5000$ , the ion ratios are less than  $N^+/H^+ = 0.05$ . This is due to the preferential dissociation of  $H_2$  ( $\epsilon_d = 4.48$  eV) over  $N_2$  ( $\epsilon_d = 9.61$  eV) indicated in Fig. A.2, where molecular and atomic number densities are given. The relatively low nitrogen ion densities observed near the nozzle exit suggest that the effective frozen gas temperature is less than  $T_g = 6000$  K.

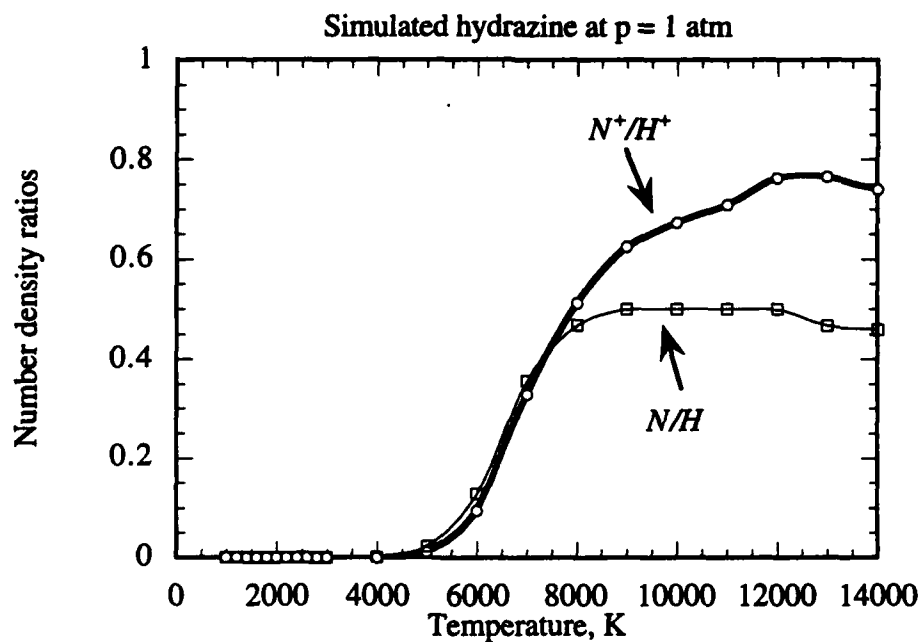


Figure A.1: Ionic and atomic number density ratios for simulated  $N_2H_4$  at  $p = 1$  atm.



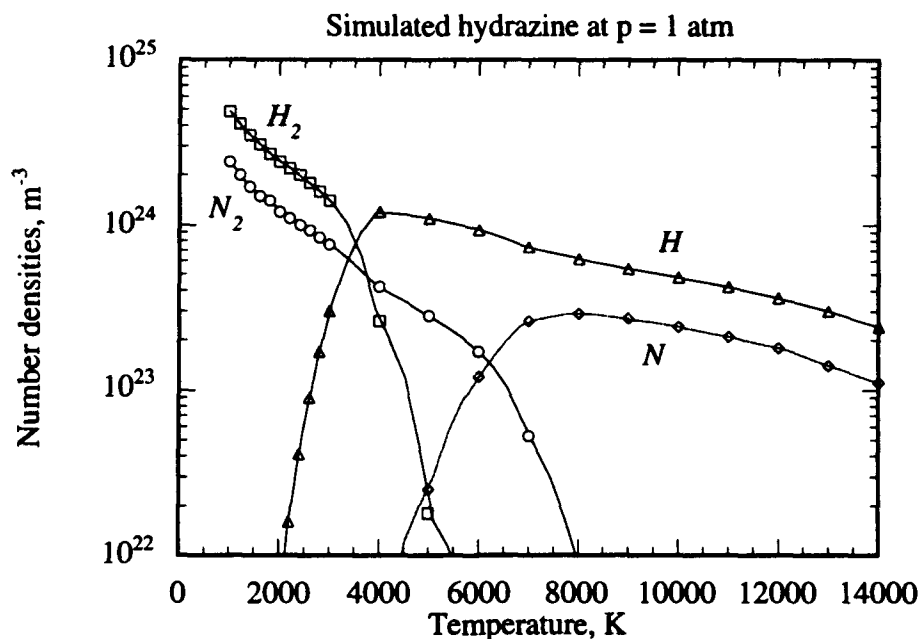


Figure A.2: Molecular and atomic number densities for simulated  $N_2H_4$  at  $p = 1$  atm.

The arcjet plasma is modeled as a highly dissociated, partially ionized, low-pressure N-H plasma, with  $T_e > T_g$  and a  $T_g$  of  $4000 < T_g < 10,000$  K in steady state. Under these conditions the hydrogen is more highly dissociated than the nitrogen and from equilibrium calculations  $n_N$  is negligible for  $T_g < 6000$  K. Furthermore, ionization by electron collision is an infrequent process.

Under these conditions, nitrogen ions rapidly lose their charge by charge-exchange collisions with hydrogen, the cross-section for which is on the same order of magnitude as N-H momentum transfer collisions. Thus:



Since the charge exchange collision rate is  $\gg$  the electron ionization rate, these two reactions balance in steady state.

Writing the volumetric charge exchange collision rate in terms of a charge exchange cross sections  $Q_{H-N^+}$  and  $Q_{N-H^+}$ , with a relative thermal speed  $v_{H,N} \equiv v_H$ :

$$[\text{collisions/m}^3\text{-s}] = n_H n_{N^+} Q_{H-N^+} v_H = n_N n_{H^+} Q_{N-H^+} v_H$$

Assuming that  $Q_{H-N^+} \equiv Q_{N-H^+}$  and combining:

$$\frac{n_{N^+}}{n_{H^+}} = \frac{n_N}{n_H}$$

For hydrazine arcjet plasmas,  $n_N \ll n_H$ , implying a low nitrogen ion density. For plasmas with low gas temperature  $T_g \ll T_e$ , and  $T_e < 10,000$  K, the nitrogen ion density is effectively determined by the gas temperature  $T_g$  and not the electron temperature. Thus as  $T_g$  falls rapidly in the nozzle by expansion and heat loss, the nitrogen ion density  $n_{N^+}$  also falls, reaching low values at the exit plane.

#### References for Appendix A

<sup>1</sup>Keefer, D., Moeller, T. and Fhodes, R., "Multiplexed Laser-Induced Fluorescence and Nonequilibrium Processes in Arcjets," AIAA Paper 94-2656, June 1994.

<sup>2</sup>Hargus, W., Micci, M. and Spores, R., "Interior Spectroscopic Investigation of the Propellant Energy Modes in an Arcjet Nozzle," AIAA Paper 94-3302, June 1994.